In-situ Powder Bed Surface Topography for Laser-Based Metal Additive Manufacturing Process Monitoring

by

Yubo Xiong

Bachelor of Science, Swanson School of Engineering, 2019

Bachelor of Engineering, Sichuan University Pittsburgh Institute, 2019

Submitted to the Graduate Faculty of the

Swanson School of Engineering in partial fulfillment

of the requirements for the degree of

Master of Science in Mechanical Engineering

University of Pittsburgh

2021

UNIVERSITY OF PITTSBURGH

SWANSON SCHOOL OF ENGINEERING

This thesis was presented

by

Yubo Xiong

It was defended on

December 7, 2020

and approved by

Xiayun Zhao, PhD, Assistant Professor, Department of Mechanical Engineering and Materials Science

Albert To, PhD, Associate Professor, Department of Mechanical Engineering and Materials Science

Tevis Jacobs, PhD, Assistant Professor, Department of Mechanical Engineering and Materials Science

Thesis Advisor: Xiayun Zhao, PhD, Assistant Professor, Department of Mechanical Engineering and Materials Science

In-Situ Powder Bed Surface Topography for Laser-Based Metal Additive Manufacturing Process Monitoring

Yubo Xiong, MS

University of Pittsburgh, 2021

Despite the rapid evolution of laser powder bed fusion (LPBF) based additive manufacturing (AM), the current LPBF systems lack the capabilities of monitoring the powder bed status such as surface topography, which could indicate the printed layer roughness and defects as well as the powder spreading uniformness. Therefore, an in-situ powder bed surface metrology method is desired to ensure built part fidelity and enhance process efficiency. In this work, we present an in-situ powder bed surface monitoring and measurement method using fringe projection profilometry (FPP). The FPP method uses a multi-phase shifting approach to obtain height profile of each layer during the LPBF process by projecting a sequence of sinusoidal varying intensity fringe patterns onto the powder bed and evaluating the fringe distortions. Measurement calibration is conducted specifically for applying FPP to LPBF process. In-situ sensor data analytics is performed with in-house codes that feature improved algorithms to estimate height profile. Experimental results with a commercial LPBF AM machine (EOS M290 DMLS) demonstrate that the developed in-situ FPP is capable of measuring the three-dimensional (3D) profile of each newly printed part layer as well as monitoring the powder bed characteristics such as surface roughness, actual powder layer thickness, and powder bed anomalies. Sample with a step surface are printed and the accompanied FPP sensor data is analyzed and validated by ex-situ Coordinate Measuring Machine (CMM). Height measurement uncertainties are explored quantitatively in this thesis.

Table of Contents

List of Figures

Acknowledgements

I would like to sincerely thank my advisor Dr. Xiayun Zhao for her supportive supervision. She taught me to think critically and has been training me to become a graduate student researcher with patience and passion. Her rich knowledge along with her style of doing research have guided me through my master study and will accompany me through the rest of my life. I would like to express my gratitude to my master thesis defense committee members: Dr. Albert To and Dr, Tevis Jacobs. I could not appreciate more for their time, help and advice on improving the quality of my thesis. I am grateful to Dr. Chaitanya Krishna P Vallbh, a lab-mate and a wonderful mentor who provides my tremendous help on revising this thesis and defense presentation. I would also thank all my former and current lab-mates in ZIM-AM laboratory: Dian Li, Tong Su, and Yue Zhang. My life of studying overseas cannot be such wonderful without their accompany. Finally, the last piece of acknowledgement goes my parents who have been supporting me financially and mentally through my life.

1.0 Introduction

Additive manufacturing (AM) offers a great capability of rapid prototyping for design purposes, in which products are fabracated by addding materials layer by layer. In recent years, AM processes are being used to manufacture industrial components. Especially metal AM can produce complex structures with compatible process conditions, which are extremely difficult to produce with conventional manufacturing processes, where parts are usually fabracated by removing material such as milling and cutting. Laser powder bed fusion (LPBF) is an advanced emerging technique that builds metallic parts into desired shapes and structures layer-wisely. As demonstrated in the figure 1-1, with LPBF process, a thin layer of metal powder are evenly distributed by recoating process onto a substrate plate. Then, a 2D slice of the product geometry for the layer are fused by selectively melting the metal powder. The substrate plate drops down and powder recoating, laser scanning and fusion are repteaded layer after layer until the final product is completed. The whole process is happened inside a chamber tightly filled with inert gas.

Even though, the metal AM can expedite the manufacturing of complex geometrical product, it has not been widely implemented in the industry because of its limitations. One of the major limitations is mechanical properties. It has been reported that the mechanical properties of the products by metal AM are not consistant . The main reason for this is because the porosity during the manufacturing process. Due to lack of real time control strategies, the laser power, scan speed, and meltpool dimensions are all source of such porosity formation. Thus, in-situ metrology has great potential of providing operators the knowledge of the manufacturing process so that make it possible for activating feedback control to compensate and even correct the detected anomalies.

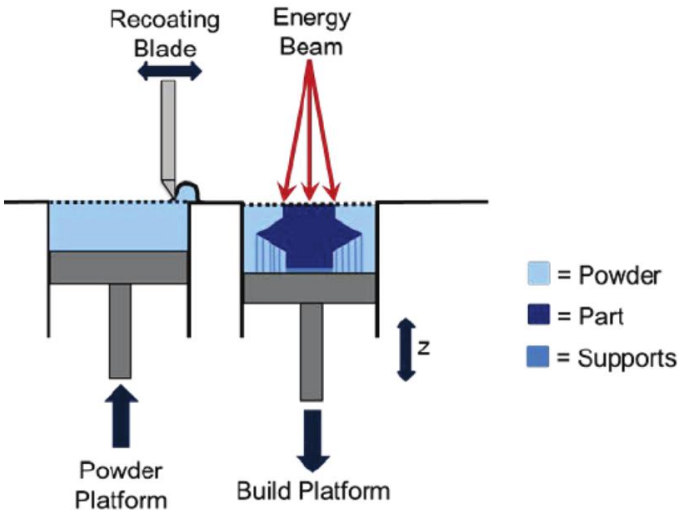

Figure 1-1. Mechanism of LPBF process (Moylan, Whitenton, Lane, & Slotwinski, 2014)

1.1 In-situ Metrology for LPBF Process

A number of in-situ metrology for additive manufacture have been researched to evaluate the formation of powder bed and solidified area. The majority is focused on high speed and high resolution camera sensors. In general, there are two classes of in-situ metrology scheme for LPBF process, including in axis system and off axis system. A in axis system refers to that the external optical devices are coaxial with the laser beam path of an LPBF system and look onto the meltpool area. Related research studies mainly include in-situ melt pool temperature profile (Hooper, 2018). and meltpool dimension estimation (Clijsters, Craeghs, Buls, Kempen, & Kruth, 2014)

An off axis system, in contrast to in axis system, is usually installed outside the building chamber. Instead of coaxially look through the laser beam, it monitors the build process through an optical window. Cases include evaluation of geometric features (zur Jacobsmühlen,

Kleszczynski, Schneider, & Witt, 2013), powder anomalies detection and classification using deep learning (Scime & Beuth, 2018) and ensembled support vector machine (Gobert, Reutzel, Petrich, Nassar, & Phoha, 2018). Figure 1-2 shows the diagram of the off-axis system developed by ZIP-AM lab, University of Pittsburgh (Vallabh, et al2020). In this work, an off axis high-speed camera is used for monitoring the powder bed area at frame rate of 500 Hz for each layer during the printing process. From the acquired images, the authors are able to identify layer-wise anomalies, observe powder bed characterization and reconstruct the 3D structure of the build part. Furthermore, the off-axis system has the potential of observing and tracking spatter due to laser sintering and motion.

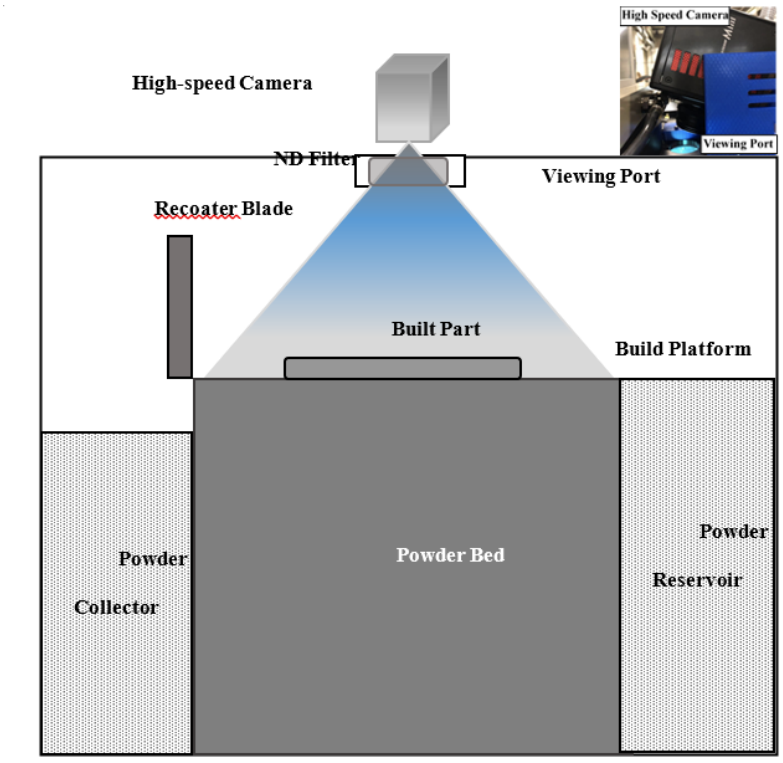

Figure 1-2. Off axis monitoring system developed by ZIP-AM lab, University of Pittsburgh (Vallabh, et al.2020)

1.2 Motivation for Developing Fringe Projection Profilometry

For each layer in LPBF process, it is essential to print with flat powder bed surface topology. However, because of the non-uniform heat transfer that happened to meltpool neighboring areas and coarse powder particles, the heat transferring performance of different regions on the built parts, and the frequent spattering of meltpool, the built pattern layers are hardly printed the same thickness. In addition, thermal distortion of built layers, as well as the widely studied laser caused defects, such as lack of fusion and keyhole effect, can also cause the non-flat surface of built layers. Such defects, as a result, greatly affect the fineness of the metal parts in roughness and are also a source of porosity. Reproducibility and quality problems are still needed to be solved by introducing precise process control techniques (Bourell, Leu, & Rosen, 2009). Thus, an appropriate profilometry is necessary to be introduced into small-scaled surface topography measurements for the LPBF system.

Coded structured light systems based on the projection of a sequence of patterns that uniquely determine each pixel in the region produced many works during the last decades including De Bruijn based techniques(Fredricksen, 1982), non-formal coding(Fechteler & Eisert, 2009), M-arrays(Etzion, 1988) and Multi-phase shifting. Fringe projection profilometry is a type of multi-phase shifting approach using projected sinusoidal varying intensity fringe patterns to reconstruct the 3D profile of a diffuse surface. Rowe and Wolford firstly proposed the idea of calculating the surface height contour using projected fringes in 1967 (B. Zhang, Ziegert, Farahi, & Davies, 2016). With many breakthroughs on technologies any algorithms, fringe projection techniques have been developed dramatically during the last decade. Numbers of fringe projection profilometry were designed to measure the 3D profile of mid- to large-sized objects (P. S. Huang,

Zhang, & Chiang, 2003). Fringe projection (FP) profilometry provides a reliable and non-destructive off-line method to learn the powder bed surface topology layer by layer.

Figure 1-3 demonstrates a comceptual setup of the powder bed surface detection using fringe projection deveoped by (Y. Liu et al., 2020). The monitoring system is implemeted in a electron beam additive manufacturing machine that comprisses an electron beam source, powder delivery system, a powder transfer stage, and the fringe projection system. The machine exibits the same in process defects that are common across all additive manufacturing machines that use powder bed, including rack damage, swelling, and porocity etc. The fringe projection system consisting of a DLP projector and a CCD camera is used for detecting the full-field 3D shape measurement of powder bed geometry.

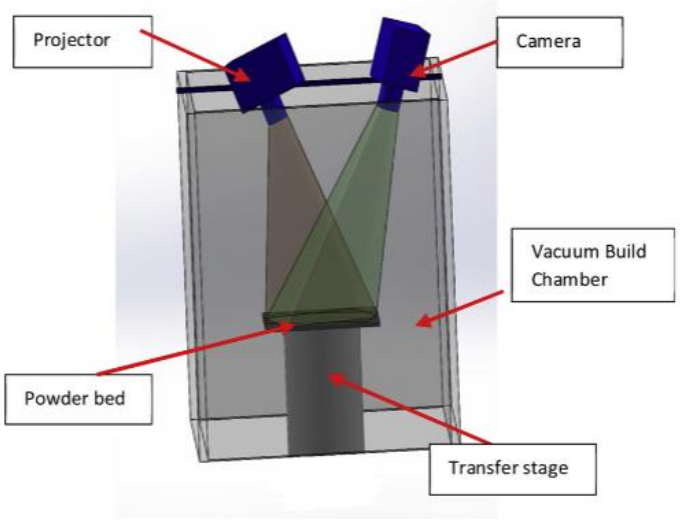

Figure 1-3. Conceptual setup of pringe projection monitoring system developed (Y. Liu et al., 2020)

A sequence of images with sinusoidal fringe patterns are projected onto the detecting powder surface. The phase value for each pixel in the images that are captured by the CCD camera is calculated through phase shifting algorithm. The mathematical formulation can be described as equation (1-1).

$$\phi(x,y) = -\arctan\left(\frac{\sum_1^N I_i(x,y)\, sin(\delta_i)}{\sum_1^N I_i(x,y)\, cos(\delta_i)}\right) \quad \textbf{1-1}$$

Where $\phi(x,y)$ is the phase value at pixel location of (x,y) in the captured image, and the unit is radians; $I_i(x,y)$ is the intensity value for each pixel. And the δ_i is the shifted step size that can be expressed as equation (1-2).

$$\delta_i = \frac{i-1}{N} \times 2\pi \quad \textbf{1-2}$$

The constant N represents the number images that are projected onto the detecting powder surface sequentially.

The small height variation on the detecting surface can be reflected by the phase change of the fringe patterns as shown in figure 1-4. A phase unwrapping algorithm is then used for evaluating the amount of deformed phase compared with a flat reference plane. In order to convert the deformed phase values for each pixel to height values, an out of plane calibration experiment

is done by evaluating the phase deformation of an object with a known height. Thus, a height map of the detecting powder bed area can be constructed as shown in figure 1-5.

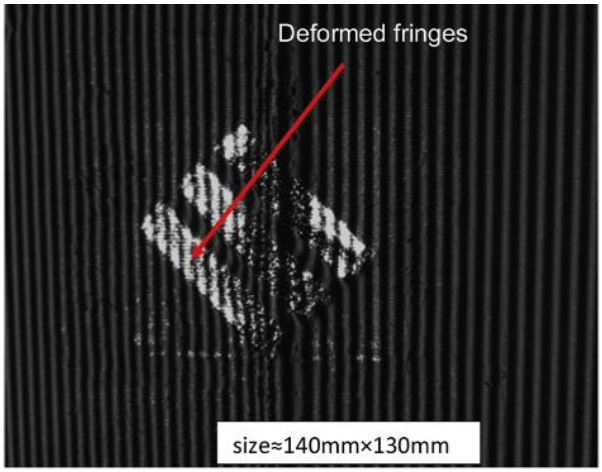

Figure 1-4. Example of camera image for deformed fringes in (Y. Liu et al., 2020)

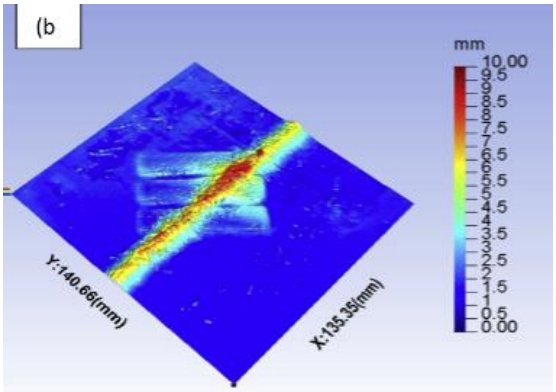

Figure 1-5. Example height map for the detecting surface in (Y. Liu et al., 2020)

Although commercial FP systems are broadly available, there are a very limited number of them meeting the micrometer level height resolution. In this project, we developed a fringe

projection profilometry for in-situ metrology of laser powder bed fusion manufacturing process. We aimed to achieve a height resolution of below 10 μm to capture height variation of the powder bed, especially the solidified region, and the actually printed layer thickness for reconstructing the printed part. Furthermore, we will try to implement the control method based on the resulted measurement to ensure the quality of printed parts.

2.0 Principal of Fringe Projection Profilometry

In section 1, we introduced the general process of LPBF additive manufacturing, the importance of implementing in-situ monitoring system, and the motivations of developing a fringe projection profilometry for LPBF. In this section, we would like to discuss the physical principals behind fringe projection profilometry and present the system that we have built in lab SB28, Benedum Hall, University of Pittsburgh. Section 2.1 briefly summarizes the current usage of fringe projection profilometry; section 2.2 derives the geometrical relationship between the target plane and the optical devises; section 2.3 presents the fringe analysis algorithms; and section 2.4 discusses the system calibration.

2.1 Application of Current Fringe Projection Profilometry

Fringe projection is usually used for a three-dimensional (3D) surface measuring. It has been reported various applications in diverse areas including human face recognition (Yagnik, Siva, Ramakrishnan, & Rao, 2005; Zhou, Li, Wang, & Shi, 2009), 3D intra-oral dental profile measurement (L.-C. Chen & Huang, 2005), and surface roughness measurement (L. C. Chen & Chang, 2008)etc. It is well-known for its ability to provide high resolution and whole field 3D map of the detected object with a non-contacted manner in a short time. As mentioned in the introduction part, a typical fringe projection system consists of a projector, a camera, and a computer to control the two units. Figure 2-1 demonstrates the geometry of the system. Measuring the 3D profile using fringe projection involves: firstly, a sequence of structured pattern, usually

using sinusoidal varied fringes and defocused binary fringes, is projected onto the target surface; secondly, the images of the projected patterns that are deformed by the object height variation is captured, and a conversion such as inverse trigonometric function is implemented to evaluate the amount of deformation in terms of phase values; thirdly, due to the discontinuity of the inverse trigonometric function, a phase unwrapping algorithm to obtain the continuous phase map over the target plane that is positively related to the height map; and finally, the system is calibrated to mapping the unwrapped phase map to the real world coordinates.

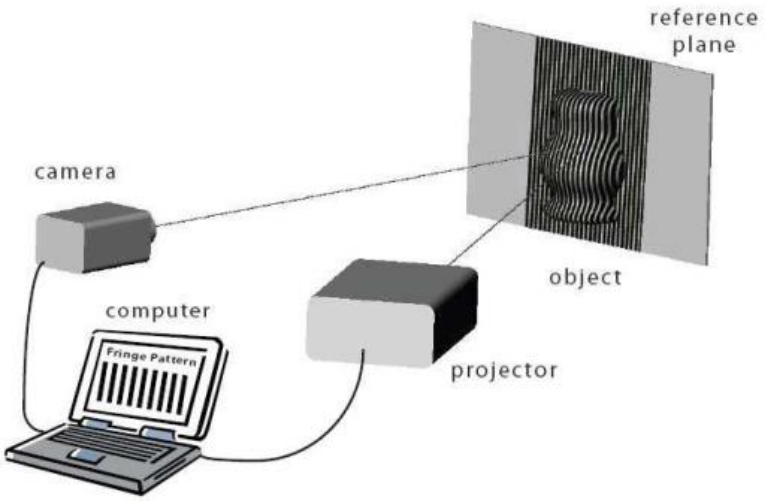

Figure 2-1. Example setup of a fringe projection system (Gorthi & Rastogi, 2010)

In (Zhou et al., 2009), the authors take advantage of the fringe projection profilometry to develop a rapid human expression measurement system. Figure 2-2 demonstrates the results from the system. The first row of figure 2-2 shows the three sinusoidal fring patterns with a phase shift of $\frac{2\pi}{3}$ between each of them that are projected onto the target face, and the second row shows the

reconstructed 3D point cloud, 3D shaped model, and the 3D model with binary texture mapping from left to right

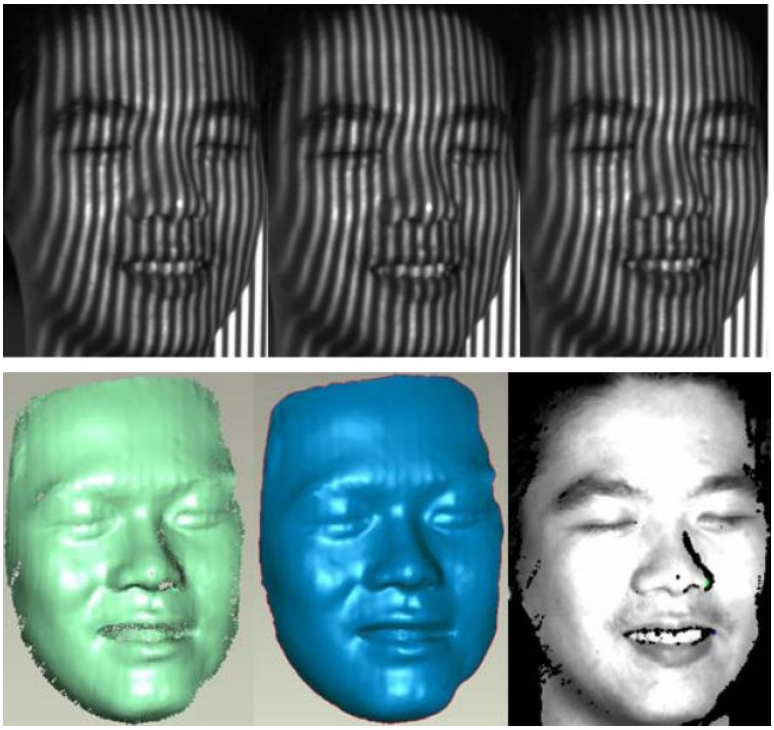

Figure 2-2. Measurement result of the human expression (Zhou et al., 2009)

2.2 Principle of Fringe Projection Profilometry

To understand the principle of fringe projection profilometry, one can view the target surface with projected fringe distortion. A shown in the first row of Figure 2-1, the fringes are bent because of the projection angle of the projector and the height variations of the face. The phase

value for each pixel that interprets the amount of distortion can be retrieved through phase shifting algorithm and phase unwrapping algorithm that will be discussed in detail in section 2.3 for fringe analysis.

To translate the phase value for each pixel, triangulation is the fundamental tool that allows retrieving the height of the target plane relative to a reference plane where the height is defined as 0. Herein, we apply the theorem of similar triangles to evaluate the geometrical relationship and calculate the height value of each camera image pixel. The 2D geometry of the fringe projection system is illustrated in the Figure 2-3. A beam of light is projected from the projector and supposed to incident at point A on the reference and the reflected beam will be capture by the camera sensor at point C. If the target object is placed on top of the reference plane (e.g. a voxel), the light beam is blocked, and the light intensity captured at the point C is actually from the pixel on projector Δx away from the original pixel. Because we are projecting sinusoidal varied fringe pattern, the Δx can be related to the phase value change Δϕ. And the relationship can be expressed as:

$$\frac{\Delta\phi}{2\pi} = \frac{\Delta x}{p}, \rightarrow \Delta x = \frac{p}{2\pi} \times \Delta\phi \qquad \textbf{2-1}$$

p is the pitch length of the projecting fringe pattern which is the distance between two adjacent fringes and also known as the spatial period of the projected fringe, and $\Delta\phi$ is the phase change in unit of radian. Hence, with a known Δx, the height value of point O can be calculated using the theorem of similar triangles between $\Delta \mathrm{P}AC$ and $\Delta \mathrm{A}OB$. The equation is expressed as:

$$\frac{H}{z} = \frac{L}{\Delta x / cos\theta_P}, \rightarrow z = \frac{H}{Lcos\theta_P}\Delta x \qquad \textbf{2-2}$$

As illustrated in Figure 2-3, the H is the distance between the optical devices plane and the reference plane; z is the height value of the target object; L is the distance between projectior and camera.

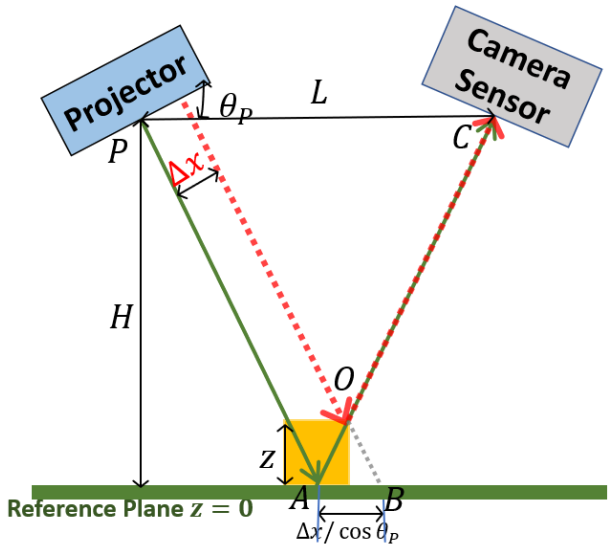

Figure 2-3. Illustration of a camera pixel capturing a light beam from the reference plane and a light beam from the object voxel. The later is a beam with a spatial shift. The schematics explains how a camera pixel's intensitry phase value encodes information of an object's voxel height

By substituting the Δx in equation (2-2), the height of the target object can be expressed as:

$$z = \frac{pH}{2\pi L cos\theta_P} \times \Delta\phi \quad \textbf{2-3}$$

Note that equation (2-3) is obtained by considering that all the points A, B, P, C, O in figure 2-2 are in the same vertical plane. However, the target object and the reference plane extend laterally, which makes the distance H not a constant but a function that varies with pixel location. Hence the height map for the target object can be expressed as:

$$z(x, y) = K(x, y) \times \Delta\phi(\mathrm{x,y}) \quad \textbf{2-4}$$

$$K(x, y) = \frac{p}{2\pi L cos\theta_P} \times H(x, y) \quad \textbf{2-5}$$

The term $K(x, y)$ reflects the sensitivity of the phase change $\Delta\phi$ relative to the height. As the parameter L and H do not change (Although the H varies with locations, the range of this variation is restricted to the chamber size of the machine), the pitch length p becomes the determinant of sensitivity. It is clearly interpreted that the pitch length needs to be smaller for measuring the powder bed of LPBF process whose height variation is in micrometer level than macroscopic measurement like human face expression identification (Zhou et al., 2009). Hence, it is necessary to select a proper pitch length for measuring different surface profile. The determination of pitch length will be discussed in section 3 for experimentation setup.

2.3 Fringe Analysis Algorithms

In the last subsection, we discussed the physics of calculating the height value for the target object. Equation (2-5) shows that the input of the model is phase deviation $\Delta\phi$. To obtain the $\Delta\phi$ from captured images required fringe analysis algorithms that include phase shifting and phase unwrapping algorithms. An intuitive way to understand the fringe analysis algorithms is to consider them as a transformation function that converts the images from intensity domain to a phase domain.

In the phase shifting algorithm, N frames of sinusoidal fringe images are projected onto the target plane. Each of the frame has a initial phase that shifted $2\pi/N$ from the previous frame. Figure 2-4 illustrsate a 3-step phase shifting fringe images. The intensity for each of the fringe image can be expressed as:

$$I_i(x,y) = B + M \cdot \cos\left(\phi(x,y) + \delta_i\right) \qquad \textbf{2-6}$$

Where i is the i^{th} frames, B is the background average intensity, M is the intensity mudulation, $\phi(x,y)$ is the phase value for each pixel, and δ is the amount of step size that is shifted between each two frames and it can be decribed as:

$$\delta_i = 2\pi\frac{i}{N}, \qquad i = 1,2,\dots,N \qquad \textbf{2-7}$$

Hence, a total of N equations in the form of equation (2-6) are used for calculating the phase value $\phi(x, y)$. A least-squre algorithm (S. Zhang & Yau, 2007). is then implemted to solve the phase value. And the result is given as:

$$\phi(x,y) = \tan^{-1}\left(\frac{\sum_{i=1}^{N} I_i(x,y) \times \sin(\delta_i)}{-\sum_{i=1}^{N} I_i(x,y) \times \cos(\delta_i)}\right) \quad \textbf{2-8}$$

To release the ambiguity of arctangent, the 2-argumented arctangent function in MATLAB is used. Note that the output of arctangent function is restricted in the range of $[-\pi, \pi]$ as shown in Figure 2-5. However, the phase of sinusoidal function should be continuous. To extend the range, phase unwrapping algorithm has to be implemted to unfold the phase jump.

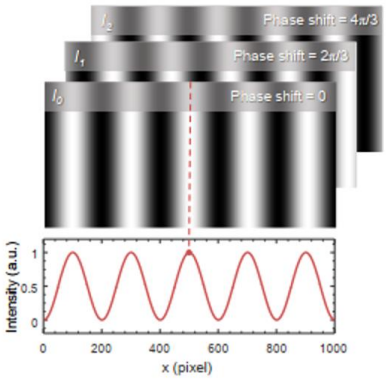

Figure 2-4. 3-Step Phase Shifting Fringe Images And The Corresponding Cross Section(Zuo et al., 2018).

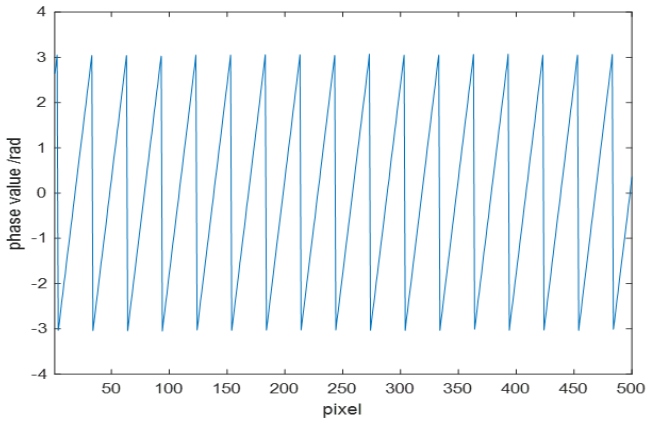

Figure 2-5. Cross Section View of Phase Map

Unwrapping phase is to simply unfold all the phase jumps. In (Itoh, 1982), the author described a fast and straightforward method to unfold all the phase jumps that are bigger that π along columns and rows correspondingly. However, this method is extremely sensitive to noise in a wrapped phase map. Thus, Q. Kemao at el. proposed a windowed Fourier filtered and quality guided phase unwrapping algorithms (Kemao, Gao, & Wang, 2008). In this algorithm, a wrapped phase map is first converted to its exponential phase field and filtered by a window Fourier transform. The filtered amplitude is used as a real valued quality map to guide the phase - unwrapping path. Different window sizes in the window Fourier transform filter are selected to solve different phase unwrapping challenges. And the filtered phase map is then used for simple phase unfolding. Figure 2-6 shows the performance of the window Fourier filtered-quality guided phase unwrapping algorithm. Although this phase unwrapping algorithm is robust, it is time - consuming especially for images from high resolution camera. Hence, this algorithm is not appropriate for in-situ monitoring using fringe projection profilometry that requires fast metrology. In (B. Zhang et al., 2016), the author introduced a reference-guided phase unwrapping algorithm.

This algorithm uses the reference phase map that is obtained from the reference plane in LPBF process using the simple phase unfolding in (Itoh, 1982) to unfold the other wrapped phase maps. To minimize unwrapping error that is from noise like saturation pixels, a third order Legendre polynomial is used to fit the reference plane. The mathematical expression is:

$$\phi_u(x,y) = \phi_w(x,y) + 2\pi \times Round\left(\frac{\phi_r(x,y) - \phi_w(x,y)}{2\pi}\right) \quad \textbf{2-9}$$

Where $\phi_u(x,y)$ is the unwrapped phase, $\phi_w(x,y)$ is the wrapped phase, ϕ_r is the reference map, and the operator $Round$ is to round the values in the bracket to a nearest integer. As the goal to measure powder bed surface in LPBF process, all the measurements are taken at around the same height level, and the height variation is extremely small (no more than 500 μm). The reference-guided phase unwrapping is very fast compared with windowed Fourier filter phase unwrapping, and it is less sensitive to noise that simply two direction unfolding in (Itoh, 1982).

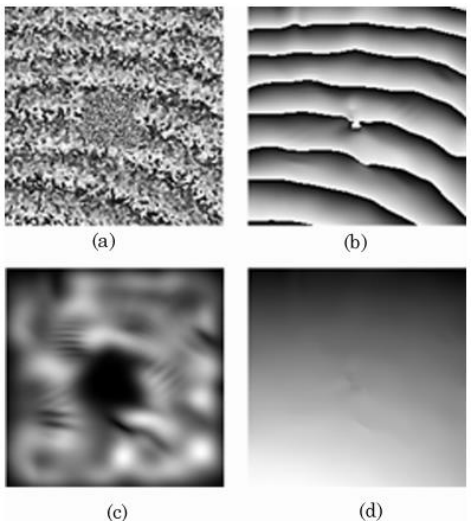

Figure 2-6. Window Fourier filter based phase unwraping: (a). a wrapped phase map (200x200), (b) the filtered wrapped phase map, (c) the filtered amplitude, (d) the unwrapped phase map. (Kemao et al., 2008)

Therefore, we first implemented the reference guided phase unwrapping algorithm. Although it is fast and less sensitive to noises, it is not free of periodical error that is coming from phase unwrapping. To further analyze the issue, we implement the reference-guided phase unwrapping algorithm to unwrap the reference plane that is the bare build plate of EOS 290 metal AM machine. Thus, the reference plane and the test plane are the same. As illustrated in Figure 2-7, the unwrapped phase along the center line from the reference-guided method exhibit some pixels that have an abruptly drop compared with their surrounding pixels. The periodical error can be more clearly observed from Figure 2-8 that is obtained by removing the inclined trend of unwrapped phase map of the test plane. To resolve this issue, we implement a two-dimensional Fourier filter to reduce the periodic phase unwrapping error, and then adding the incline trend back to create the unwrapped phase map. Figure 2-9 shows the performance of the two-dimensional Fourier filter. To further view the performance of applying the Fourier filter in phase unwrapping

algorithm, figure 2-11 shows the in-situ topography of two fatigue bars. It is clearly observed that the periodical error reduced a lot. Hence, the procedure for unwrapping the phase map is concluded as (Figure 2-10): firstly, we apply Ioth's simple two-dimensional unfolding algorithm to a flat reference plane; secondly, we apply a third order Legendre's polynomial fitting to the unwrapped phase of the reference plane; thirdly, we take the reference unwrapped phase map into equation (2-9) to calculate the unwrapped phase map for the target plane; lastly, we remove the incline trend of the unwrapped phase map, implement the two-dimensional Fourier filter to the detrended phase map, and add the incline trend back to create the unwrapped phase map. Once the unwrapped phase map is created, the phase deviation $\Delta\phi(x, y)$ in equation (2-5) can be calculated as:

$$\Delta\phi = \phi_u(x, y) - \phi_r(x, y) \qquad \textbf{2-10}$$

Where $\phi_u(x, y)$ is the unwrapped phase map of the target object, and $\phi_r(x, y)$ is the unwrapped phase of reference plane.

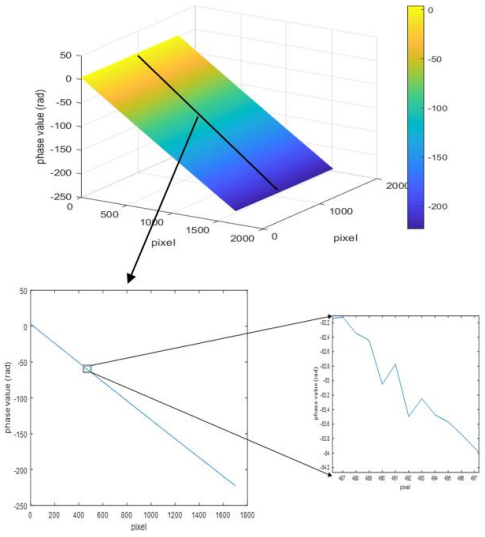

Figure 2-7. Cross section veiew of the unwrapped phase using reference-guid algorithm

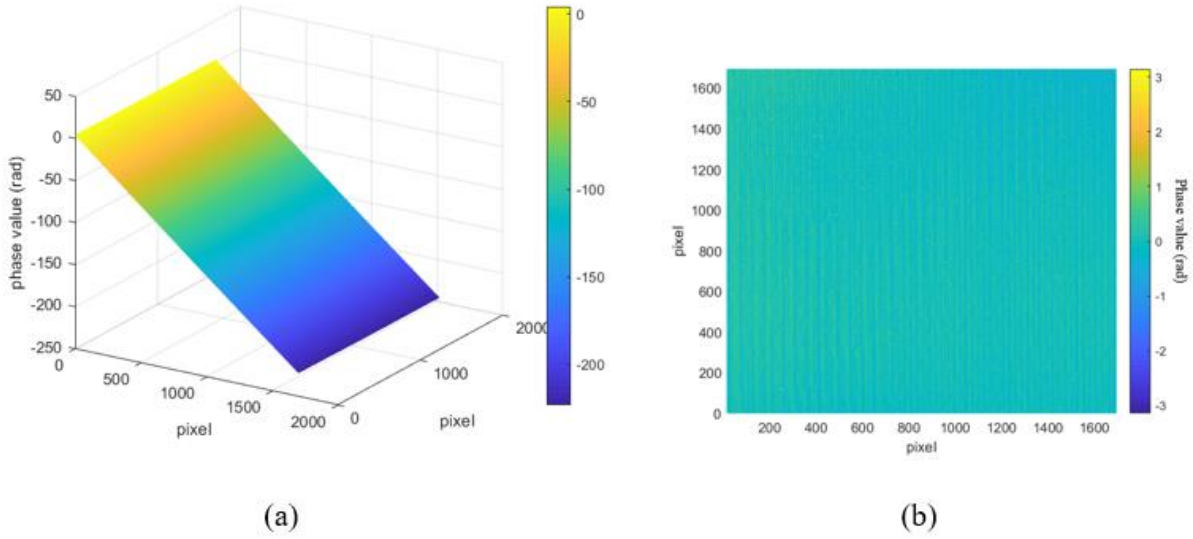

Figure 2-8. Unwrapped phase map using refrence-guid algorithm. (a) the original unwrapped phase map of the test plane. (b) the top view after removing the inclined trend of the unwrapped phase map.

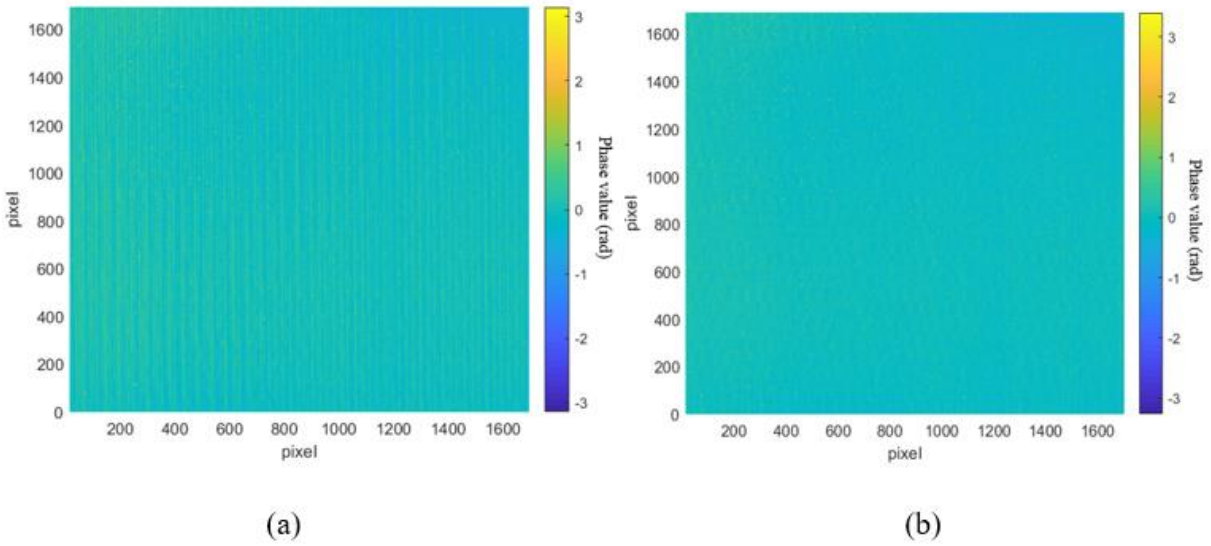

Figure 2-9. Performance of the two-dimentional fourier filter(2DFF). (a) before applying the 2DFF, (b) after applying the 2DFF.

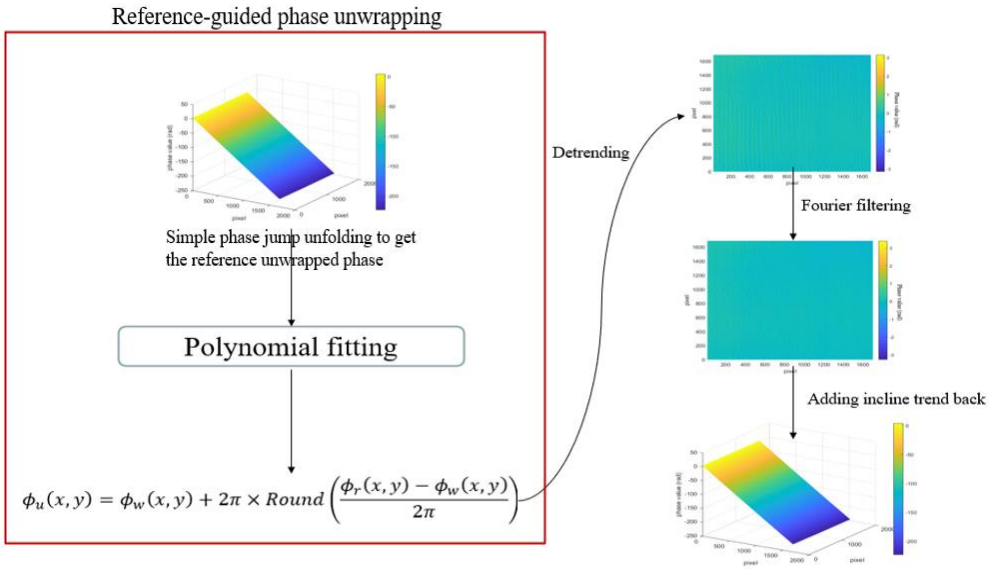

Figure 2-10. Modified phase unwrapping procedure.

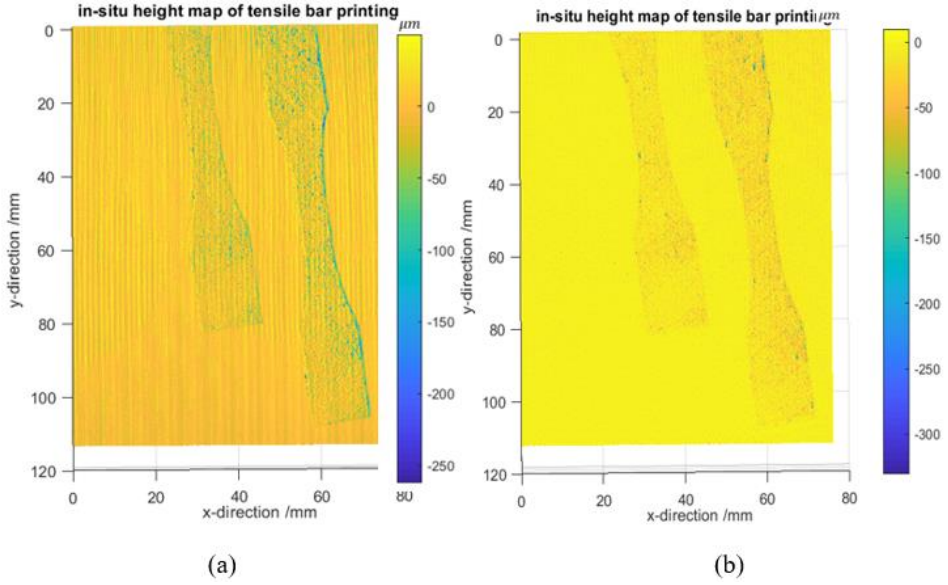

Figure 2-11. The heihgt profile using reference guid phase unwrapping (a), and the heihgt profile using modified phase unwrapping (b).

2.4 System Calibration

In subsection 2.2, we derived the model for calculating height profile of a target object from phase deviation $\Delta\phi$, and in subsection 2.3, we discussed fringe analysis and determined the $\Delta\phi$. As shown in equation 2.5, to obtain the height value, the parameter $K(x,y)$ needs to be determined. System calibration is the procedure of constructing the bridge from phase value to height value. Calibration techniques have been widely studied. Generally speaking, they can be categorized into photogrammetry-based calibration (H. Liu, Su, Reichard, & Yin, 2003; Reich, Ritter, & Thesing, 2000; S. Zhang & Huang, 2006) and least-square calibration (L. Huang, Chua,

& Asundi, 2010). Photogrammetry is to measure sensor coordinates and globally match the partial views. It is the reconstruction of three-dimensional coordinates by two or more images that are taken from different angles. As for the least-square approach, it calibrates the phase-to-height conversion for the in-plane and out-of-plane separately. The in-plane calibration is done by using a flat grid plate. The grid distance is accurately measured manually. A perspective-correction algorithm is applied to remove the image distortion due to camera viewing angle. The out-of-plane calibration is achieved using the relationship between phase and height. In (Jia, Kofman, & English, 2007), the authors summarized linear model and nonlinear model for phase to height conversion. As the height variation of powder bed for LPBF process is much less than the distance between powder bed and projector-camera plane ($z \ll H$), the calibration method used in our fringe projection system is least-squre approch with linear model. For in-plane calibration, a transformation matrix is created to correct the distorsion of acquired images. For out-of-plan calibration, a plot is created by recording the height values and phase values in ten different positions to determine the $K(x, y)$ in equation (2-5).

In-plane calibration is the process of converting the height map from a pixel scale to a x-y millimeter scale. This is achieved by acquring the image of a calibration grid plate with accurately measured dimensions. In our case, we placed a flat plate with grid pattern onto the powder bed. A projective transformation matrix $T_{9\times9}$ is created by mapping the coordinates of four corners of the grid plate with the non-orthogonal image taken from CMOS camera. The perspective corrected coordinate can be expressed as:

$$[x', y', z'] = T_{9\times9}[x, y, z] \qquad \textbf{2-11}$$

Where $[x, y, z]$ is the original image space, while $[x', y', z']$ is the coordinate in orthogonal planar object space (Wolberg, 1990). Figure 2-12 shows the grid plate and illustrates the process of such image perspective correction. The same transformation matrix is used for any other image correction from the system. The dimension of each square is $5mm \times 5mm$. By counting the number of pixels in a known length, the ratio of pixel scale to x-y millimeter scale is $(38\mu m \times 38\mu m)$ per pixel. This in-plane resolution can be further improved by adjusting the camera to zoom into certain area:

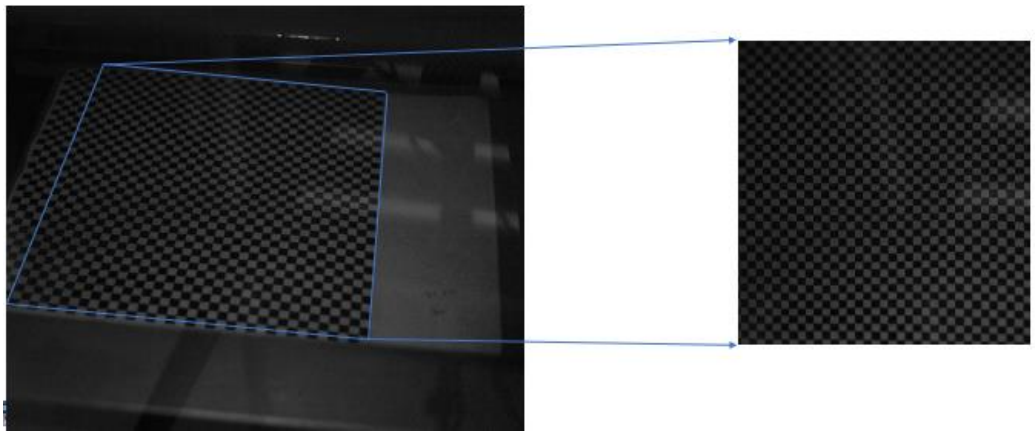

Figure 2-12. Example of in-plane calibration (image perspective correction).

The out-of-plane calibration is the process of converting an unwrapped phase map to a height map. In another words, it is a process of determining the parameter $K(x, y)$ for each pixel in equation (2-5). This is done by moving a flat reference plane over a range that covers the height variation of the powder bed. For our system, we use the first powder layer as the reference plane and move the build stage to ten different height positions with increments of 0.1 mm. We define the first height position as 0 mm and move the build stage down to -0.1 mm, -0.2mm, …, -1.0 mm.

the unwrapped phase maps are calculated for the ten height positions. For each pixel, the phase values and their corresponding height are fit to a straight line, and the inverse of slope, which has unit of millimeter per radian (mm/rad), is obtained and assigned to $K(x, y)$ in equation (2-5). Figure 2-13 shows the plot of height versus phase for the pixel at the center of the field of view, and Figure 2-14 shows the $1/K(x, y)$ map ever the whole area.

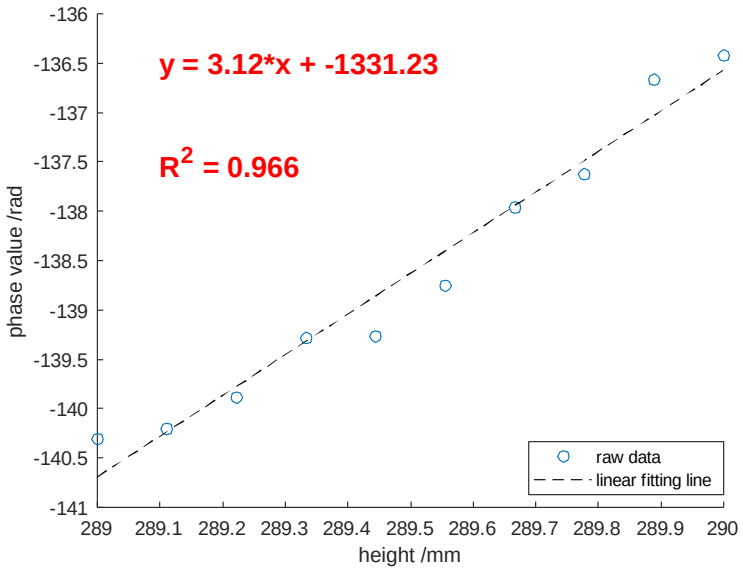

Figure 2-13. Phase value versus height at the center pixel (the slope of the fitting line represents the inverse of K.

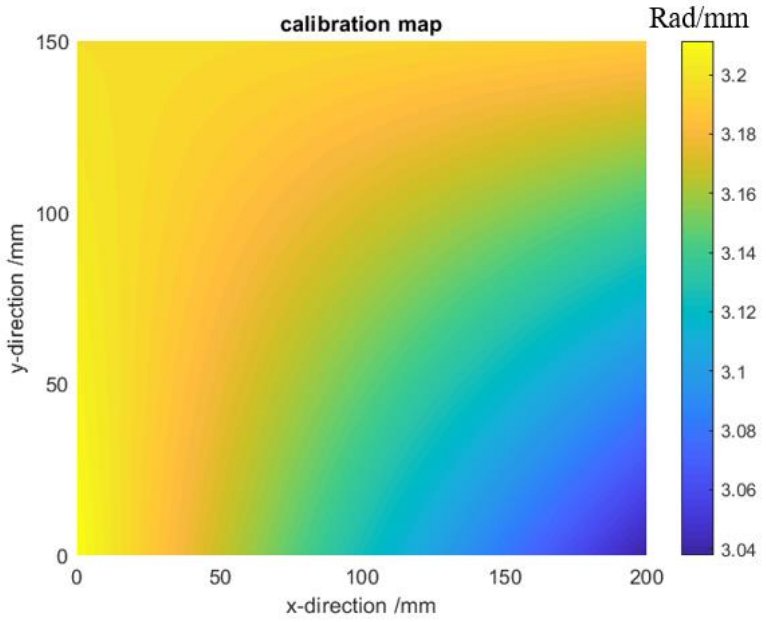

Figure 2-14. 1/K(x,y) map

2.5 Projector-Camera Calibration

The combination of projector and camera is not a linear system. The intensity (gray level) of images captured by camera is usually not proportional to the light intensity (gray level) that is projected by the projector (see Figure (2-15(a))). Hence, if a sinusoidal pattern is projected onto a flat surface, the image viewed by camera would be distorted due to this nonlinearity relationship. This distortion will contribute to harmonic error in unwrapped phase calculation and the height profile as shown in Figure 2-15. Thus, it is necessary to calibrate the projector-camera relationship to reduce harmonic error in the height profile measurement.

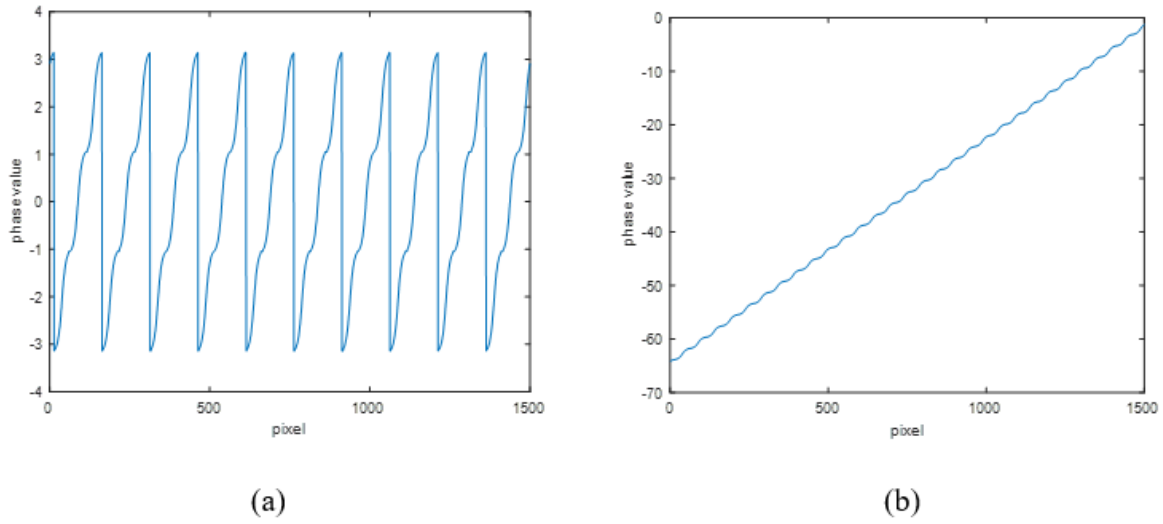

Figure 2-15. Example of distortion of phase value due to nonlinearity, (a) wrapped phase, (b) unwrapped phase.

To calibrate the projector-camera relationship, a curve of intensity (gray level) acquired by camera as a function of projected intensity (gray level) is created. We did this by projecting a sequence of uniform intensity images through the projector onto a flat surface. As camera has 8-bit digitized output, thus an intensity range of 256 gray level, we project 230 uniform intensity images that the intensity value varies from 10 to 240 because this range will be used for sinusoidal fringe. Even though a uniform intensity image is projected, the acquired irradiance is not uniform in the viewing area because of randomly distributed over saturated pixels. Thus, we take the average irradiance of the whole viewing area. Figure (2-16 (a)) shows the plot of acquired intensity (gray level) versus projected intensity (gray level) with a polynomial curve fitting to the raw data. We want this curve to be a straight line so that the projected intensity (gray level) matches the acquired intensity (gray level). Thus, we need to modify the acquired intensity. We did this by creating a calibration curve inversed (Figure (2-16 (b))) from the polynomial fitting curve of the

raw data (Figure (2-16(a))) with respect to the x=y line. For images that are acquired by the camera, the intensity (gray level) at each pixel is mapped onto the calibration curve (Figure (2-16(b))) and replaced by the corresponding output. Figure (2-17) shows the acquired fringe pattern after this modification. Figure (2-18) shows the relationship between the projected intensity (gray level) and the acquired intensity after calibration. As it is clearly observed, this calibration yields a linear relationship between the input projected intensity (gray level) and the output acquired intensity (gray level). Hence, for further experimentation, we modify the acquired intensity (gray level) based on this calibration curve for the projector-camera calibration.

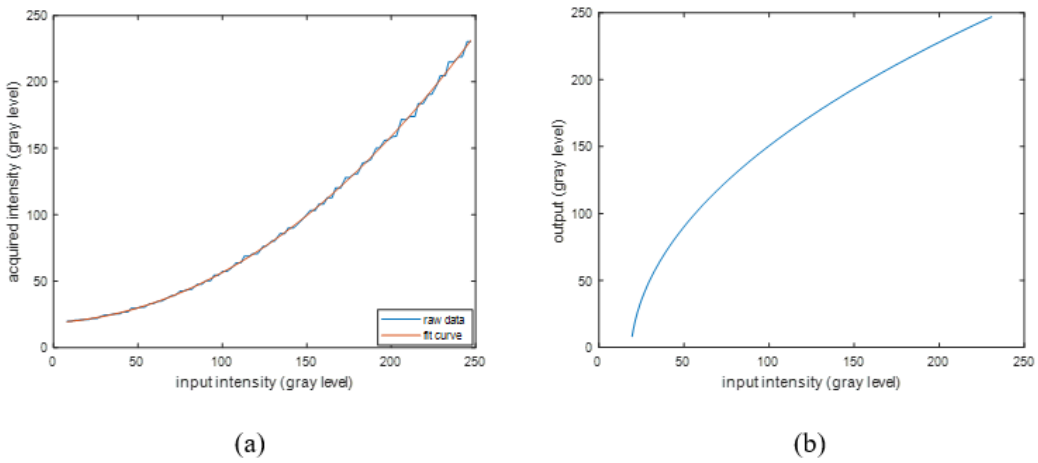

Figure 2-16 Non-linear relationship between projector and camera, (a) raw response of the camera with a polynimial fitting curve; (b) the inverse curve of the fitting.

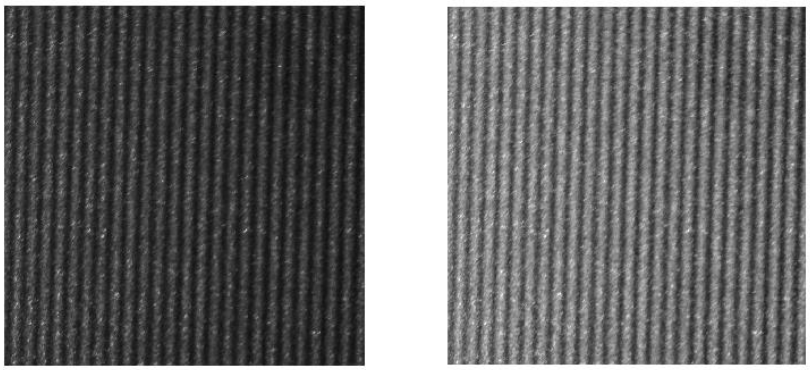

(a) (b)

Figure 2-17. Acquired fringe pattern before (a) and after (b) calibration.

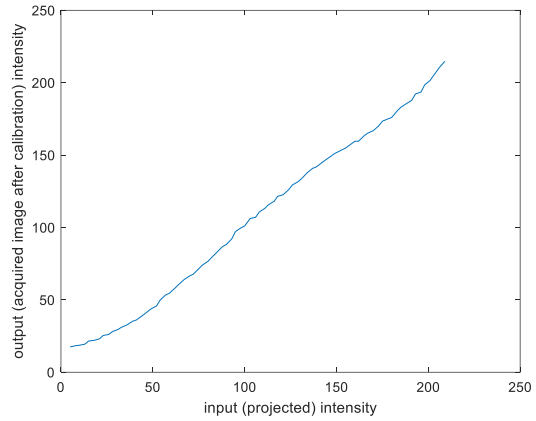

Figure 2-18. Projector and camera relationship with projector-camera calibration (input is the projected intensity after calibration, and output is the acquared intensity after calibration.

To further evaluate the performance of the projector-camera calibration, we projected a sinusoidal fringe pattern onto a flat surface. To view the improvement, we obtained the Fourier frequency spectrum of the center line intensity for both images. Figure 2-19 shows the Fourier

frequency spectrum of the sinusoidal pattern that is input for projecting. Figure 2-20 shows the comparison with and without the projector-camera calibration.

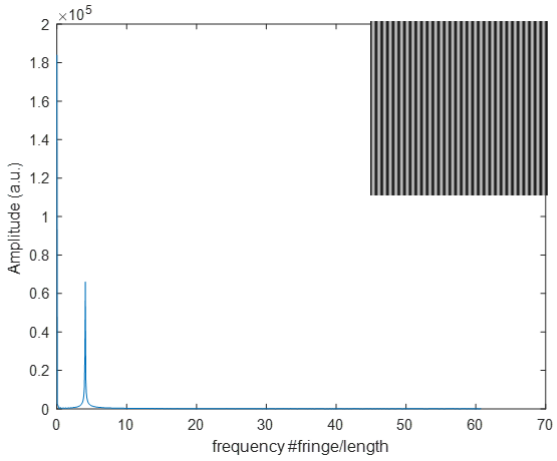

Figure 2-19. Fourier spectrum of the sinuoidal fringe pattern input to the projector used for projecting

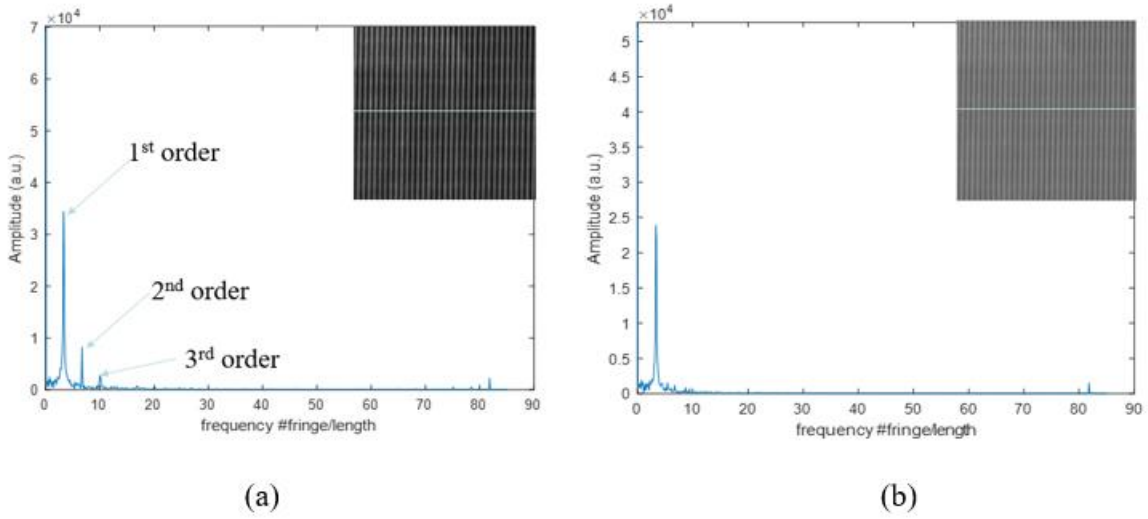

Figure 2-20. Fourier spectrum of acquired images from the camera, (a) before and (b) after the calibration.

Before the calibration, we can observe two more peaks (2nd order and 3rd order) that are related to harmonic error. After the calibration, only the primary (1st order) peak is left. And the

Fourier spectrum of the calibrated image is similar to that of the sinusoidal pattern generated by computer.

2.6 Summary of The Developed Fringe Projection Profilometry Method

To summaries the procedure of implementing the developed fringe projection system on LPBF metal AM, figure 2-21 presents the flowchart. Firstly, the optical devices projector and camera are calibrated so that they have a linear relationship, meaning the light intensity projected matches the intensity acquired. A 3-step sinusoidal fringe pattern is projected onto the target surface, and images are acquired. Then, the unwrapped phase map is calculated using the phase shifting algorithm (equation 2-7). The modified phase unwrapping algorithm with 2D Fourier filter (equation 2-9 and figure 2-10) is applied to unfold the discontinuity due to the use of inverse trigonometric function. Hence, the phase deviation $\Delta\phi(x, y)$ in equation 2-5 can be evaluated. A system calibration including out of plane calibration and in plane calibration is performed to obtain the $K(x, y)$ value in equation 2-5. Therefore, the height value $z(x, y)$ for each pixel can be calculated.

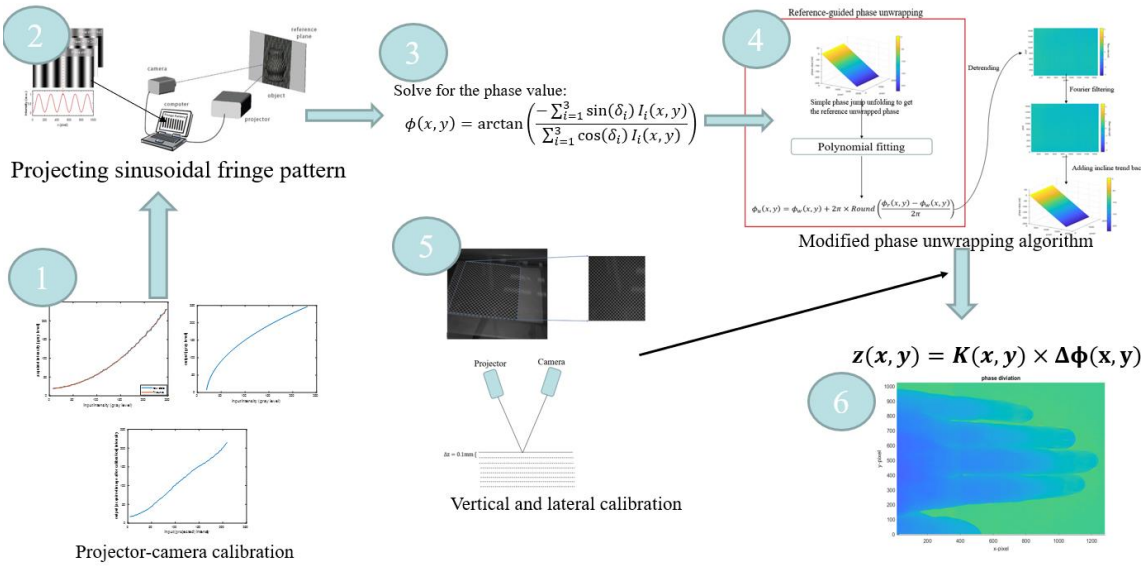

Figure 2-21. Flow chart of surface topography using the developped fringe projection system.

3.0 Development and Experimentation of Fringe Projection System

In section 2, we discussed the physical principles behind fringe projection profilometry by deriving the geometric relationship, applying fringe analysis algorithms, and conducting system calibrations. In this section, we will be describing the fringe projection system that we established on EOS 290 metal AM machine in Benedum Hall SB28, University of Pittsburgh with emphasis on the hardware including projector and camera, experimentations, operating algorithms, and result analysis. Subsection 3.1 summarizes the hardware information; Subsection 3.2 describes the experimentations; Subsection 3.3 presents the in-situ fringe projection measurement results on LPBF process.

3.1 Hardware Selection

The LPBF metal AM machine under our investigation is EOS M290 DMLS that is designed and made by EOS brand (See Figure (3-1)). It has a building chamber of $250 \times 250 \times 325\ mm^3$, with a 400-Watt laser, allowing a fast and cost-effective production of metal parts directly from CAD data. Three are three circle windows on top of the machine that allows us to mount optical devises to perform monitoring. A CMOS camera was instilled at the center window, while a projector was installed at the right window. Figure (3-1) shows a picture of the EOS M290 DMLS machine with fringe projection system installed on the top.

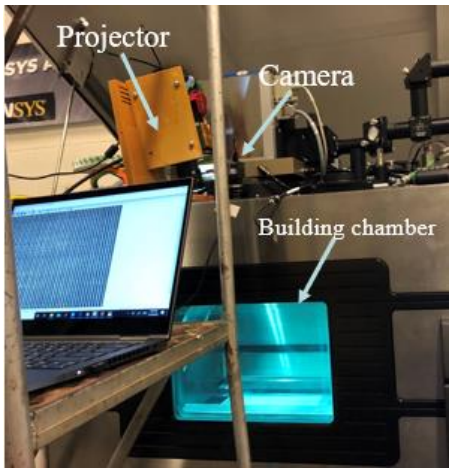

Figure 3-1. Picture of the fringe projection system on the EOS M290 DMLS machine

Figure (3-2) shows the geometrical drawing with specified dimensions and distances of the fringe projection system and the powder bed.

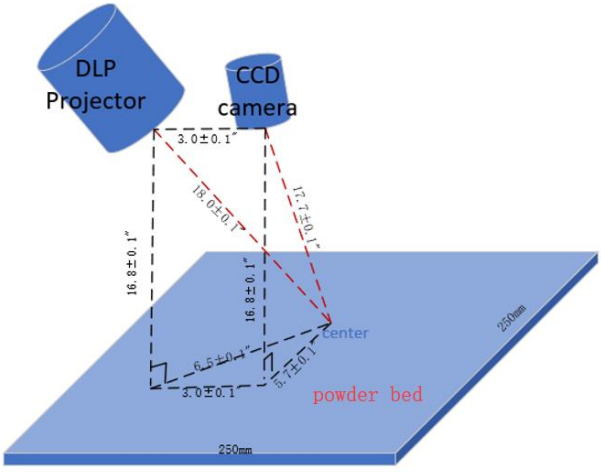

Figure 3-2. Geometrical drawing with labeled dimensions of the fringe projection system

In fringe projection profilometry, the sinusoidal fringe pattern is projected by a projector. Thus, to measure the whole powder bed area, the projected image should cover $250 \times 250\ mm^2$. The printing area is approximately 457 mm (18 in) away from the projector as shown in Figure (3-2). The aspect ratio (length/width) for majority of commercial screen is 16/9. The throw ratio that is defined as the distance over image width for such requirements needs to be at least $457mm/250\left(\frac{16}{9}\right)mm = 1.23$. For this reason, we select the DLP LightCrafter Display 4710 EVM-G2 that has an adjustable throw ratio from 1.29 to 1.39 by the adjustable zoom lens. The resolution of the selected projector is 1920 pixels by 1080 pixels and the micromirror pitch (pixel size) is 5.4 μm. In order to achieve a high in-plane resolution, the camera used for image acquisition should have a high pixel number, as the more pixels insure more data points in a single image and thus higher resolution. Hence, we select the Flea3 USB3 CMOS camera. It has a resolution of 4000 pixels by 3000 pixels and the camera sensor format is 1/2.3'' whose dimension is $6.17 \times 4.55\ mm$. To select an appropriate camera lens, focal length that is related to the distance and imaging area needs to be calculated. The mathematical equation can be expressed as:

$$f = \frac{d}{1 + \frac{L}{w}} \qquad \textbf{3-1}$$

where f is the focal length, d is the distance between lens and object, L is the width of field of view, and w is the camera sensor width. In our case, the field of view is $250 \times 250\ mm$ and the distance d is approximately $450mm$. Thus, the focal length is calculated as $10.8\ mm$. We choose a 12M pixel lens with adjustable focal length from $3mm$ to $10\ mm$ because the peripheral area of

powder bed is usually not the printing area and, with this lens, we can zoom in to smaller area for more accurate height profile measurement.

3.2 In-situ LPBF Process Measurement Experimentation and Results

To achieve a higher measurement resolution, the pitch length of the projected fringe pattern needs to be extremely small ($p < 1\,mm$) (B. Zhang et al., 2016). As the projected image is approximately $250 \times 250\,mm$, the number of projected fringes must be larger than 250. Thus, we generate 300 fringes in a single image from MATLAB as shown in figure 3-3 that is used for the projection. One more consideration is the Nyquist sampling theorem. The minimum sampling rate for a sinusoidal wave needs to be at least 2 pixels per cycle. In our case, as the resolution in the horizontal direction for the projector is 1080 pixels, it gives sinusoidal fringe pattern of 4 pixels per cycle, which is feasible for Nyquist sampling theorem.

In LPBF process, it takes three steps to finish printing for each layer. Firstly, the recoating blade run across the build stage and spreads a layer of powder. We then take the FP measurement of the newly formed powder layer as the reference plane for the printed area height profile measurement. Secondly, laser starts to scan and print certain area, after which we take the second FP measurement of the same field of view that contains the printed area. Lastly, the build stage is moved down $40\,\mu m$ to prepare the next layer powder deposition. This is when we take the third FP measurement. The reason of doing the third measurement because we want to evaluate the exact layer thickness of each pixel that can be calculated by subtracting the height profile obtained from the third measurement (after the build stage moves down) of the last layer (layer #n-1) from the second measurement (before the build stage moves down) of the current layer (layer #n).

Figure 3-4 shows the procedure. For each FP measurements, a 3-step phase shifting sinusoidal fringe pattern is projected as shown in figure 3-4. For each measurement, three fringe patterns with different phases (figure 3-3) are projected sequentially.

The process of obtain the topography for the layer is concluded in the flowchart (figure 3-5). Firstly, the unwrapped phase map of reference plane (first measurement) and the printed layer (second measurement) is obtained using the phase shifting algorithm and phase unwrapping algorithm. The phase deviation map is calculated by subtracting the reference unwrapped phase map from the printed layer phase map $\Delta\phi(x, y)$. Then, the calibration result $K(x, y)$ is plugged to compute the height value for each pixel. For analyzing the layer thickness, it is computed by subtracting the topography of the last printed layer after build stage moves down from the surface topography of the current layer. Note, the first 14 layers will be cut away when removing the build part from the bare stage, so we just need to calculate the layer thickness after 14^{th} layer.

Figure 3-3. 3-step sinusoidal frigne patterns.

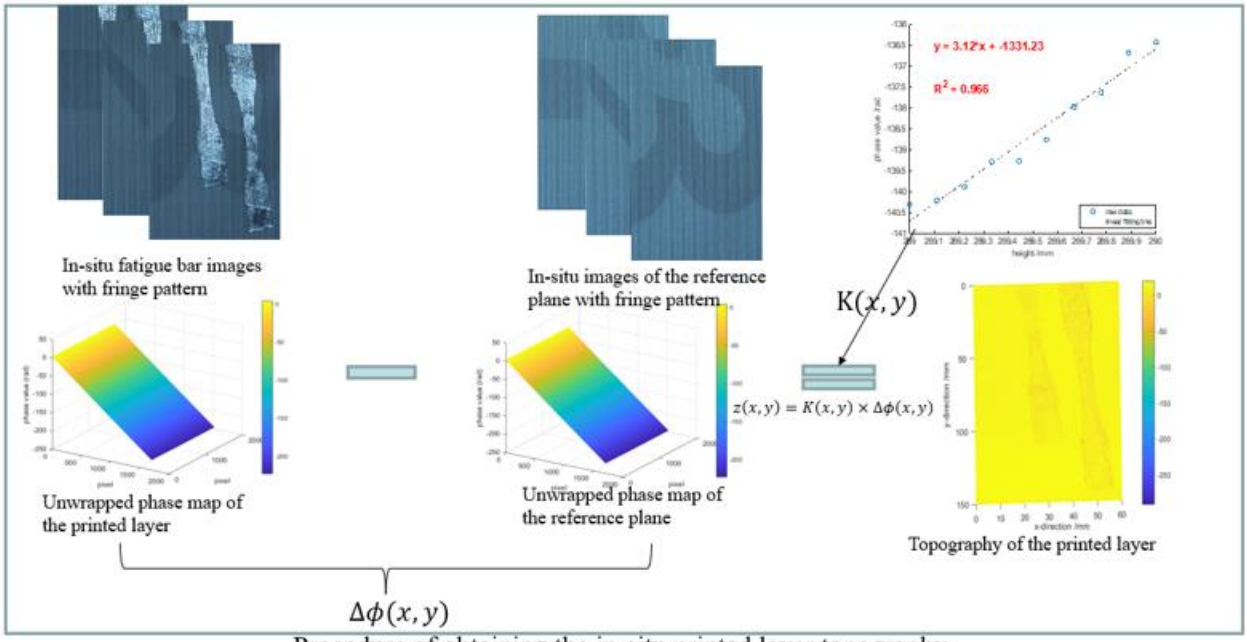

Procedure of obtaining the in-situ printed layer topography

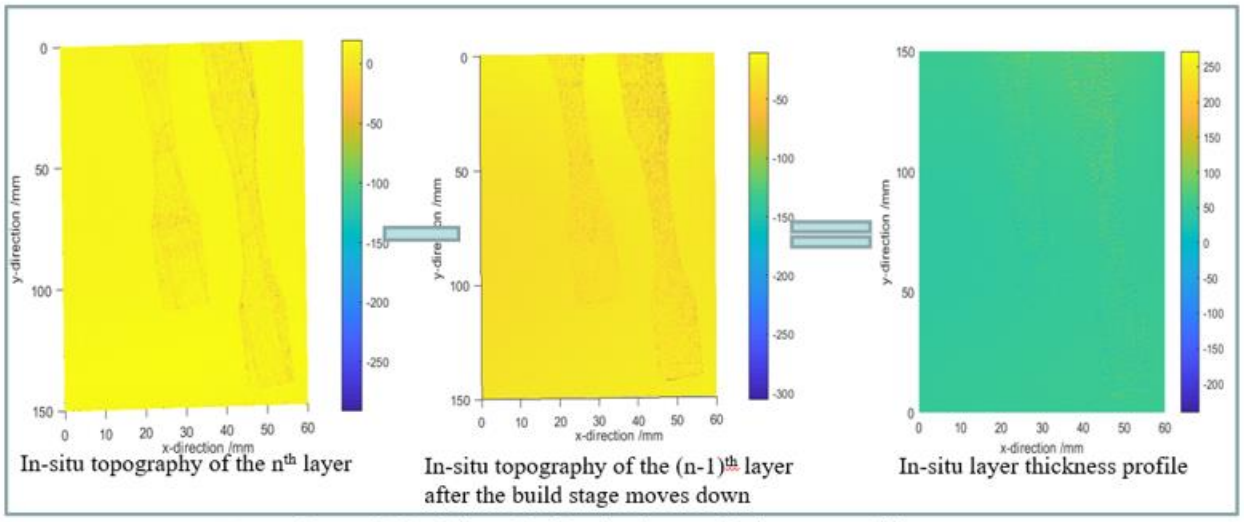

Procedure of obtaining the in-situ layer thickness profile

Figure 3-4. FP measurement Procedure of obtaining the in-situ printed layer topography and layer thickness profile.

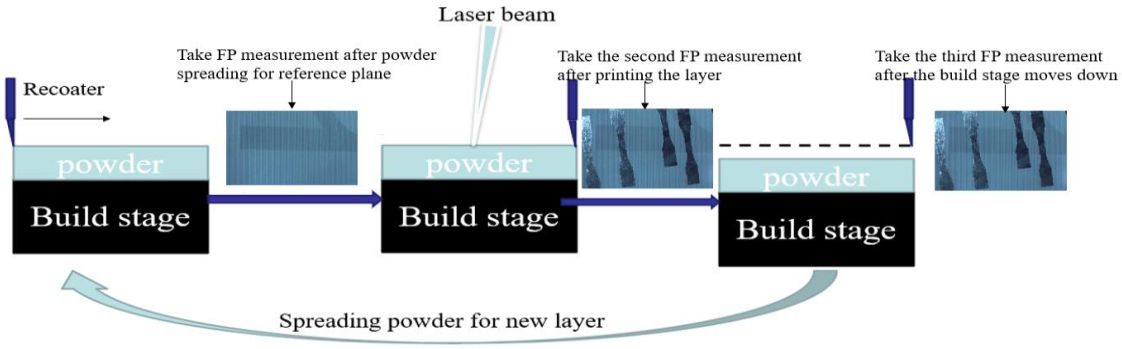

Figure 3-5. Procedure for taking the in-situ data.

To test the performance of the developed fringe projection system, 5 fatigue bars are manufactured using the EOS M290 DMLS AM machine. The process parameters are laser power 285 W, scan speed 1000 mm/s, powder layer thickness 40 μm, and the material is Inconel 718. The hatching pattern and scan strategy vary for each layer to avoid stress concentration. The part build orientation of the fatigue bars on the powder bed is shown in figure 3-6. And the in-situ powder bed image along with the projected fringe pattern is shown in figure 3-7. An area of $110 \times 150\ mm$ is captured by the CMOS camera. Four out of the five fatigue bars are covered in this area. Because there are a lot of over saturated pixels in the bottom two fatigue bars and they are a little defocused due to manual mistakes in lens adjusting, we are mainly focused on analyzing the upper two fatigue bars in this preliminary study. The in-situ height profile of the fifth layer is shown in figure 3-8 as an exemplar illustration. Figure 3-8(a) shows the raw in-situ image, figure 3-8(b) shows the in-situ image after projector-camera calibration, figure 3-8(c) shows the height profile using the reference-guide phase unwrapping model, and figure 3-8(d) shows the height profile using the modified phase unwrapping calculation (figure 2-9). It is observed that periodic

error appears in the height profile if we directly apply the reference guide phase unwrapping model. Using the modified phase unwrapping algorithm can reduce the periodical error to certain extent. In the height profile, the height variation of hatching pattern can be observed that is usually not usually extracted from photography using camera. The average height of the fused area is lower than the powder surface because of solidification shrinkage, which is reflected in the in-situ height profile.

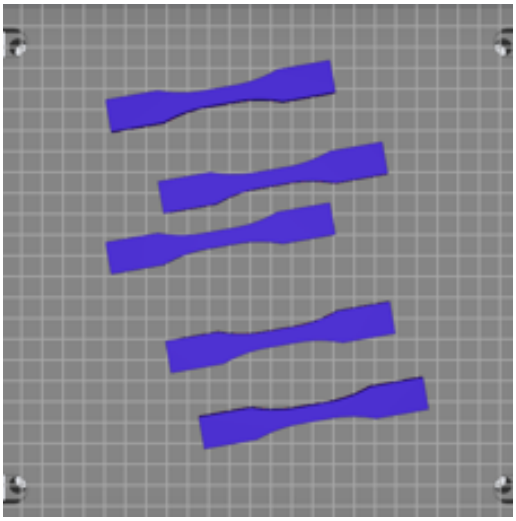

Figure 3-6. build orientation for the fatigue bars.

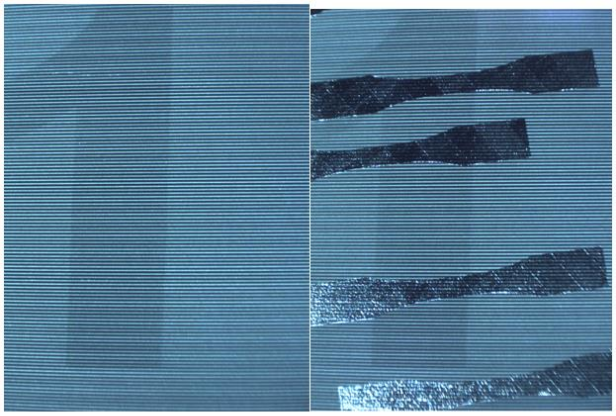

(a) (b)

Figure 3-7. Representative in-situ images for the fartigue bar printing with projected fringe pattern. (a). reference plane; (b) after laser fussion.

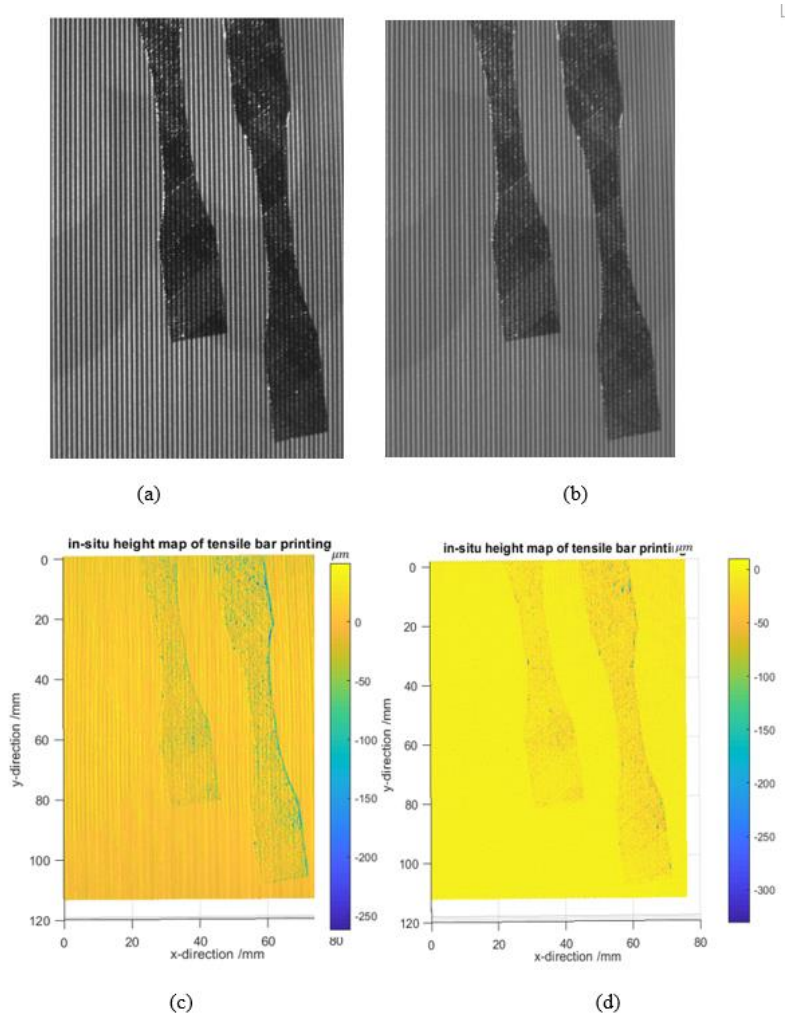

Figure 3-8. Representative in-situ measutrement using FP system: raw in-situ image (a) and after projector-camera calibration (b), the heihgt profile using reference guid phase unwrapping, and the heihgt profile using modified phase unwrapping (d).

In this experiment, a total of 92 layers out of 108 layers (total number of layers for the five-fatigue bar printing) are recorded. As shown in figure 3-4, during the printing process for each layer, we take three measurement. The third one is regarding to the layer thickness analysis. The layer thickness profile of the fused area is obtained by subtracting the height profile of the third measurement (after the build stage moves down) from the second measurement (before the build stage moves down). The average value for each layer thickness profile is plotted along with the

corresponding layer number, shown in figure 3-9. The average layer thickness for the 92 layers is $40.27\ \mu m$ that is close to the preset layer thickness $40\ \mu m$. A simple validation of the in-situ measurement can be done by comparing the overall printed part thickness from the estimation from FP measurement and the manual measurement. We add all the layer thickness profiles to see the final printed part thickness of the printed fatigue bars (figure 3-10). The average height of the fatigue bars area is 3.96 mm. Considering we missed 16 layers, the approximated overall thickness is $3.96mm + 16\ \times 40\ \mu m = 4.60\ mm$. And a rough manual measurement of the printed fatigue bar shows the thickness of 4.68 mm. This comparison shows that our fringe projection system is promising in terms of measuring height profile. A more concrete height profile validation will be done by comparing the height profile of in-situ measurement of the last layer with ex-situ measurement of the printed surface, and the ex-situ measurement specification is shown in the Future work section of this thesis.

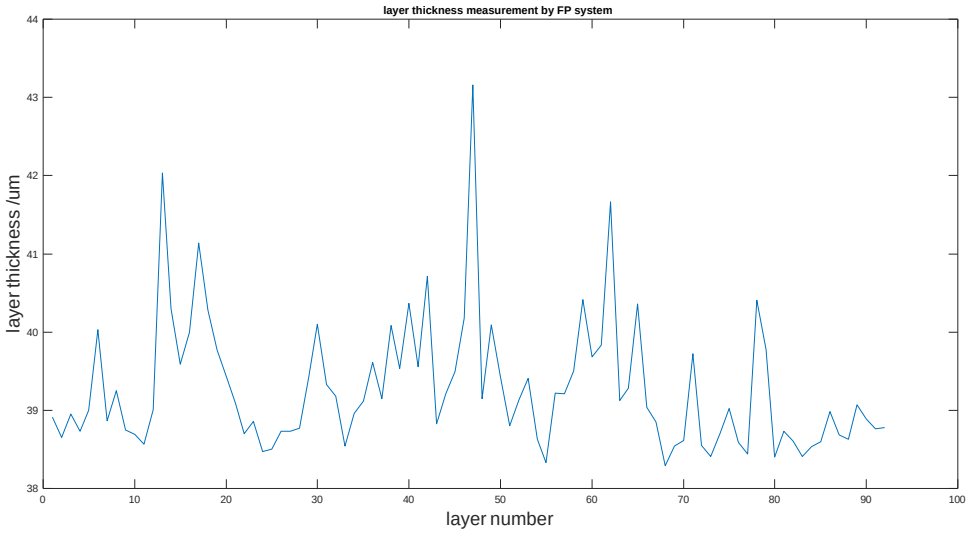

Figure 3-9. Fused area layer thickness.

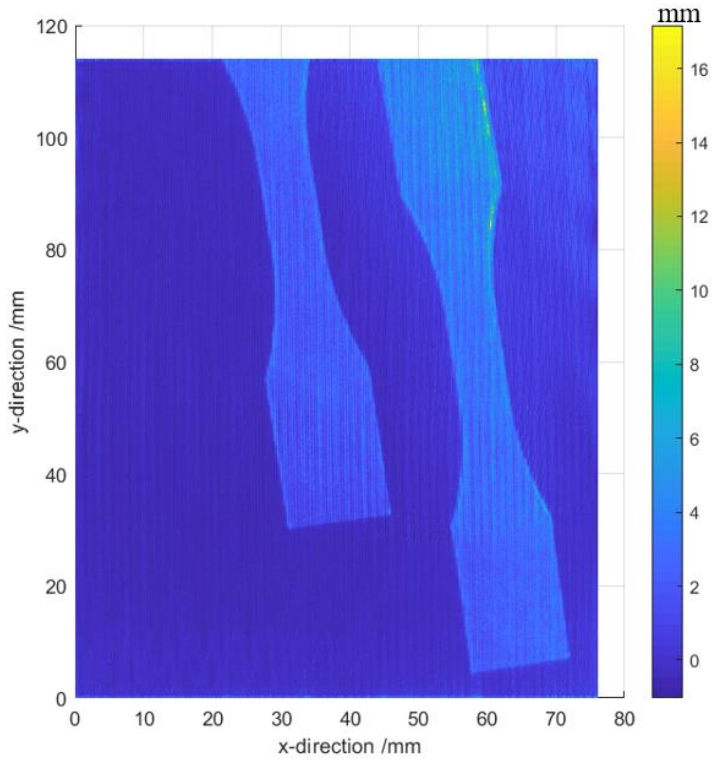

Figure 3-10. Height profile of adding all the thickness profile (92 layers).

4.0 Ex-situ Height Measurement Validation

In section 3, we discussed the selection of projector and camera, procedure of applying FPP measurement, and the in-situ height profile measurement of the fatigue bar printing. Furthermore, we did a preliminary validation by evaluating the layer thickness profile and the thickness of the final printed part. In this section, we will be discussing the ex-situ measurement of step surfaces to validate the height measurement capability and explore the height resolution of our FP system. Section 4.1 shows the experimental design of the object with step surface; section 4.2 presents the comparison of ex-situ height measurement between FPP and Coordinate Measuring Machine (CMM).

4.1 Experiment Design: Step Surface

Once the fringe projection system is developed, we need to think about the measurement capability of the system, assure the height measurement results, and explore the smallest feature that can be accurately measured. To achieve these goals, we printed two samples with step surface using the EOS M290 DLMS metal AM machine as shown in figure 4-1 (the unit of the dimensions shown in the figure is millimeter). One of the samples has a step increment of 40 μm (This is the default printing layer thickness of the EOS machine) and the other one has a step increment of 10 μm (This is the smallest layer thickness of the EOS machine and the height measurement resolution that we want to achieve). The surface profile of the printed sample with 40 μm step increment is measured using both our FP system and a coordinate measuring machine (CMM).

The CMM measures the geometry of the sample by sensing discrete points on the step surface with a probe. As shown in figure 4-2. The picture was taken when the probe of CMM is scanning the 40 μm step surface. The height measurement resolution of CMM is 12 μm. Hence, it cannot provide us an accurately measurement of the step surface with 10 μm step increment. In section 7, We will discuss a more accurate profiler to capture the 10 μm step increment.

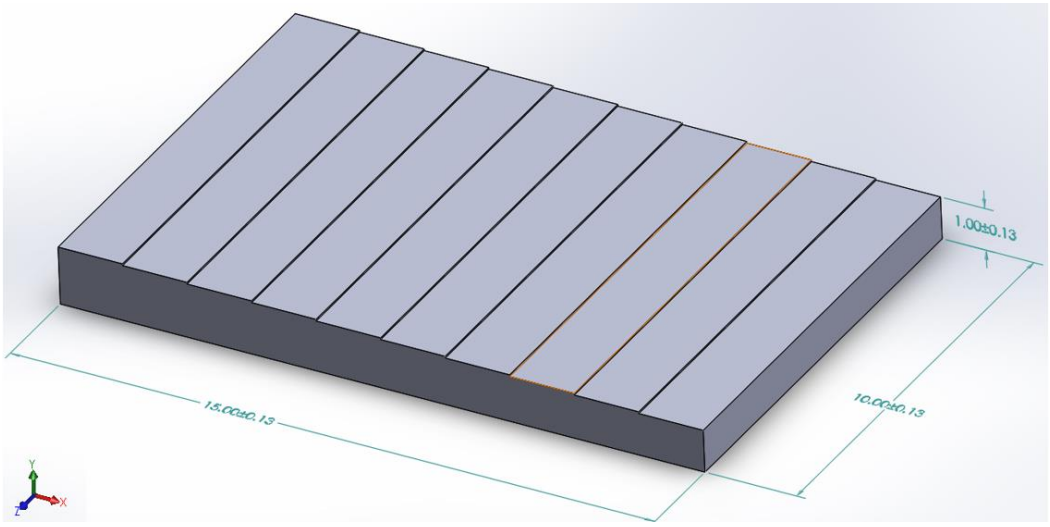

Figure 4-1. 3D drawing of the sample with step surface.

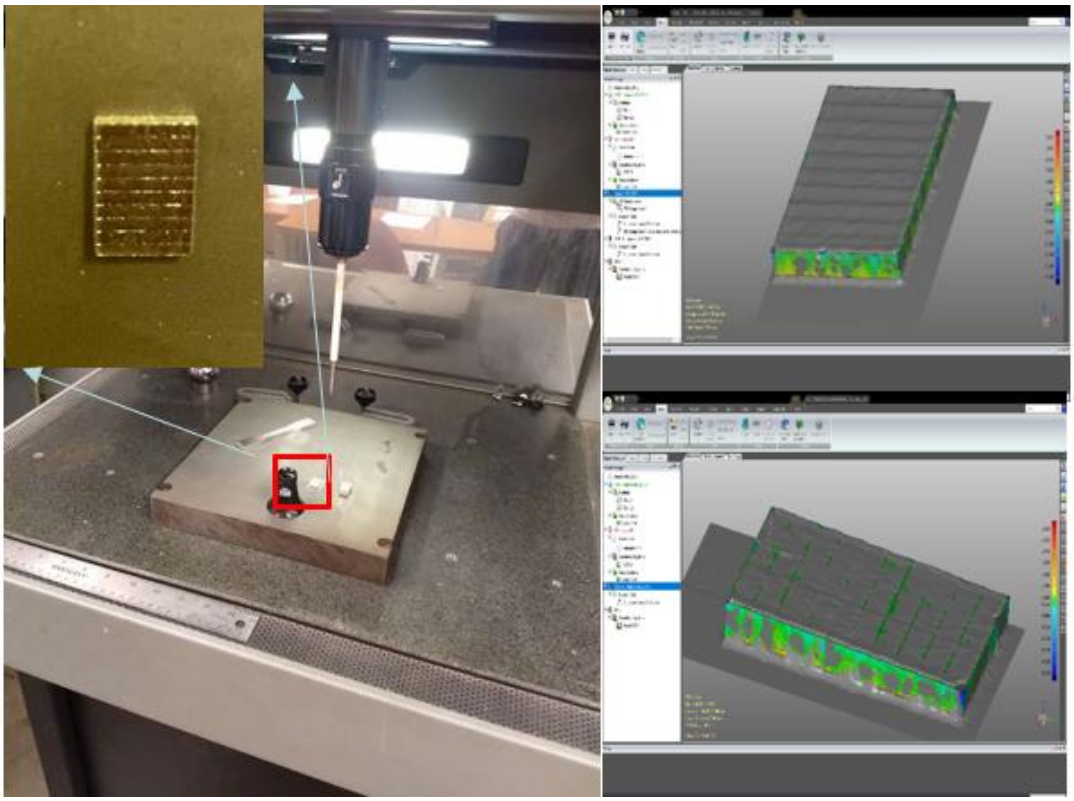

Figure 4-2. CMM measuring process.

4.2 Ex-situ Height Measurement of Step Surface

To demonstrate the performance of our FP system, the ex-situ measurement results of the step surface ($40\mu m$) are shown and compared with the topography generated by the CMM. For the FP measurement, three-step shifting sinusoidal fringe patterns are projected onto the bare build plate with printed samples (the powder is cleaned for the measurement). The fringe analysis and the developed phase unwrapping algorithms (in section 2) are implemented. Figure 4-3 shows

fringe pattern and ex-situ topography of the step surface using our FP system. Figure 4-3 (a) is the raw ex-situ image with projected sinusoidal fringe pattern, figure 4-3 (b) shows the ex-situ image after the projector-camera calibration (projector and camera linear correction, details are shown in section 2.5), and figure 4-3 (c) is the ex-situ topography of the step surface ($40\mu m$). We can clearly see the steps from the topography, from which we can have preliminary conclusion that our FP system can achieve a height measurement resolution of 40 μm. The height of the substrate of the sample is 1 mm (as shown in figure 4-1). Once the light (fringe pattern) is projected from the left, it is observed from the image that there is a shaded area on the right side of the sample. We are not able to capture the height information from the shaded area and this is the reason why the height values of this area in the topography (figure 4-3 (c)) do not make sense. However, in this measurement, we are only concerning about the step surface and, for the in-situ image, the shadow effect becomes insignificant because the height variation across the powder bed is very small (in micrometer level). Furthermore, our newly proposed dual projection for FPP will solve this issue (the details are shown in section 6).

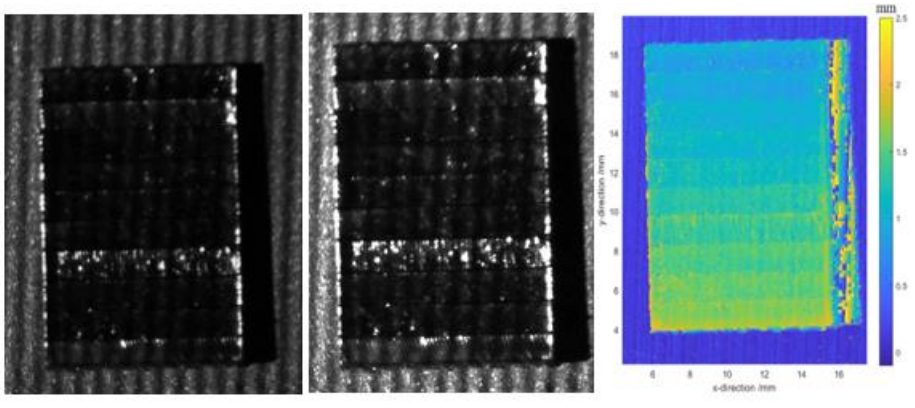

Figure 4-3. FP measurement results: (a). The raw image with fringe pattern; (b). The image after projector-camera calibration; (c). The height map created by our FP system.

Step #	Average height value (mm)	Increments (mm)
1	1.4510	
2	1.4662	+0.0152
3	1.5130	+0.0468
4	1.5434	+0.0304
5	1.5806	+0.0372
6	1.7331	+0.0525
7	1.7754	+0.0323
8	1.8051	+0.0397
9	1.8422	+0.0371
10	1.8987	+0.0465
Average step increment		+ 0.0375
Standard div.		0.0103

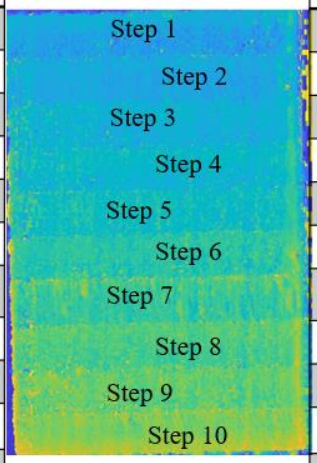

Step #	Average height value (mm)	Increments (mm)
1	1.4520	
2	1.4675	+0.0155
3	1.5118	+0.0443
4	1.5420	+0.0302
5	1.5711	+0.0291
6	1.7282	+0.0571
7	1.7459	+0.0177
8	1.7978	+0.0519
9	1.8336	+0.0358
10	1.8779	+0.0443
Average step increment		+0.0362
Standard div.		0.0136

Figure 4-4. Average step value and step increments, left table: average height value evaluated arithmatically; right table: average height evaluation using robust regression.

To quantitively view the step surface, we evaluate the average height of each step using arithmetic calculation and using robust regression. For arithmetic calculation, we simply add the height value in each pixel for each step and divided by the number of pixels. We can see from the right-hand side table in figure 4-4, that the average step increment is 37.5μm with a standard deviation of 10.3 μm. For the robust regression, it is an iterative procedure that minimizes the impact of outliers on the coefficient estimation. The right-hand side table in figure 4-4 shows the average height values and step increments using robust regression. The average step increment is 36.2 μm with a standard deviation of 13.6 μm. The average step increment calculated from the two methods are closed to each other, meaning the outliers (abnormal height value due to over saturated pixels) in the topography have minor effect in the average calculation.

Figure 4-5 shows the topography measurement result using CMM. At the bottom, the parameters show the average step increment of 35.9 μm with standard deviation of 25.9 μm. This

CMM measurement is a good validation of our FP system. The measurement results are very close to each other, and the relative percentage error of the average step increment is 0.83% ($\frac{36.2\mu m - 35.9\ \mu m}{36.2\ \mu m}$). To better view the comparison of the topography from the two measurement systems (FP and CMM), we plot the two topography in the same figure (figure 4-6). Figure 4-6 (a) shows the isometric view and figure 4-6 (b) shows the side view, in which the scatter represents the CMM measurement and the color map represents the FP measurements. We can see especially from the side view that the two topography matches very well with each other.

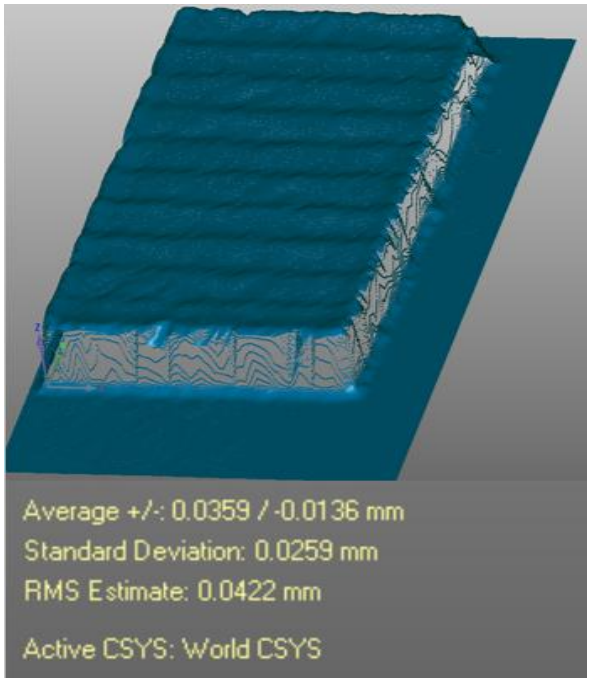

Figure 4-5. CMM measurement result, the parameters at the bottom shows the average step increment, standard deviation, and root mean square estimation.

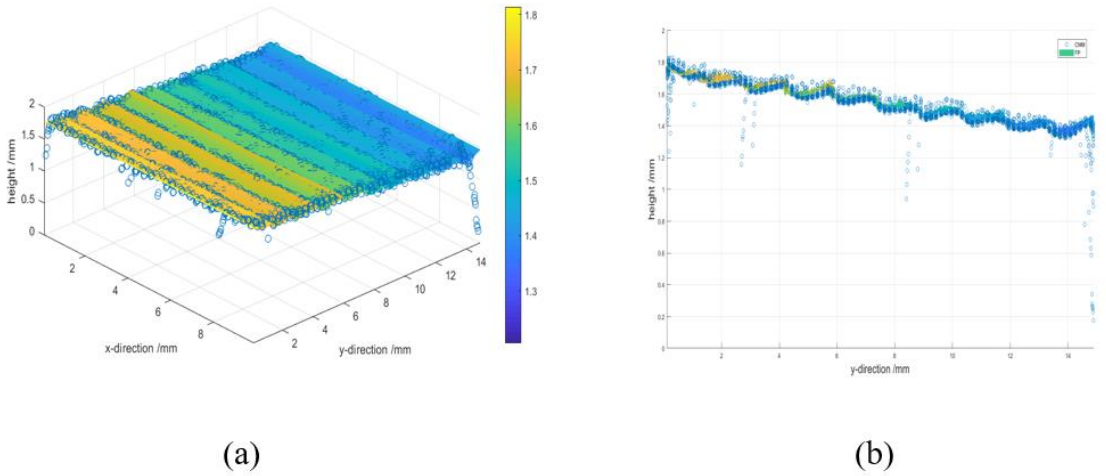

(a) (b)

Figure 4-6. Topography of the step surface using CMM (scatter) and FP (color map). (a) isometric view, (b) side view.

For our FP system, the number data points we have for the step surface area is 296,784, while for the CMM, the number of data points is 6,488, much smaller than the FP system. In order to create an error map for the FP system from the comparison between the two system, we decrease the data points using "downsample" function in MATLAB (Signal Processing Toolbox) to match the data points from CMM measurement. Then, we can get the error map by subtracting the height profile by CMM from FP. The error maps (both isometric view and side view) are shown in figure 4-7. We can see that the error varies from -0.05 mm to +0.05 mm. The root mean square (RMS) is calculated as 0.019 mm. The drawback of using this down sampling is that the x-y coordinates of the two topography are not exactly match with each other.

Another way we tried to quantitatively compare the topography of the two systems is evaluating the amplitude distribution (Leach, 2014). In our case, it is defined as the probability distribution of the height value, providing the probability that a profile of the surface has certain height at certain position. Figure 4-8 and figure 4-9 represent the number of data points at each

height value (interval (bin size) of 0.007 mm, a total 100 intervals) for both FP measured topography and CMM measured topography of the step surface (40 um). The probability for each height value is evaluated by dividing the number of data point at each height value by the total number of data points. Figure 4-10 and 4-11 show the probability distribution of the height value for the 40-um step surface measured by CMM and FP correspondingly. To compare the two distributions, a Chi-square test is applied. The Chi-square score can be expressed as:

$$\chi^2 = \sum_{i=1}^{100} \frac{(FP_i - CMM_i)}{CMM_i} = 65.56 \qquad \textbf{4-1}$$

Where FP_i represents the probability density from FP measured topography at the i-th bin (interval), and CMM_i represents the probability density from CMM measured topography at the i-th bin (interval). The degree of freedom for chi-square test is calculated as the number of intervals minus one. The critical chi-square value at the confidence level of 95% is 77.93 larger than the calculated chi-square score. Thus, the two probability distributions should be the same. So, we can conclude that the ex-situ measurement of our FP system is valid.

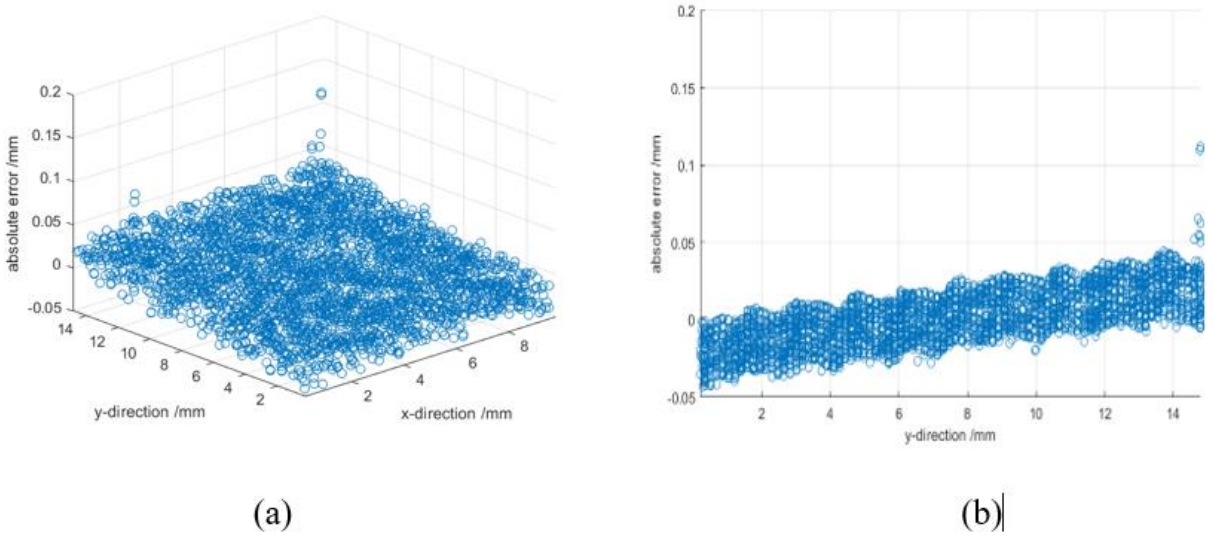

Figure 4-7. Error map created by substracting the heihgt profile by CMM from FP. (a). isometric view, (b). side view.

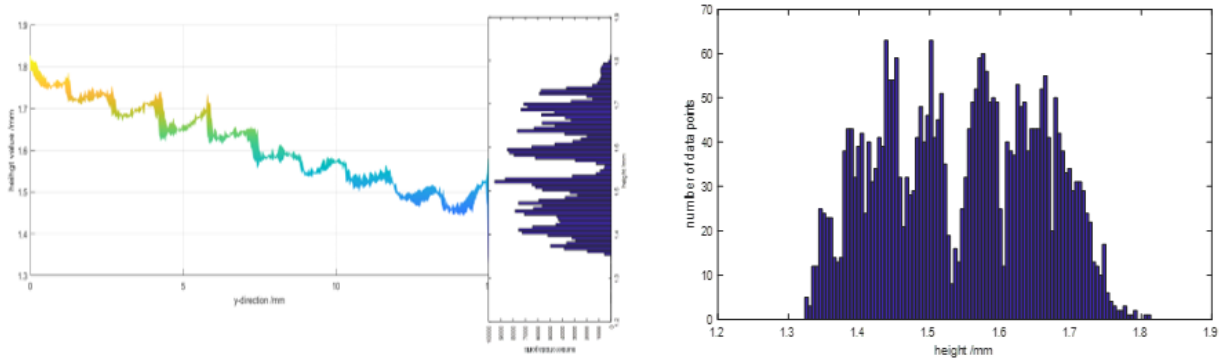

Figure 4-8. Histogram: number of data points at each height value for the topography of CMM.

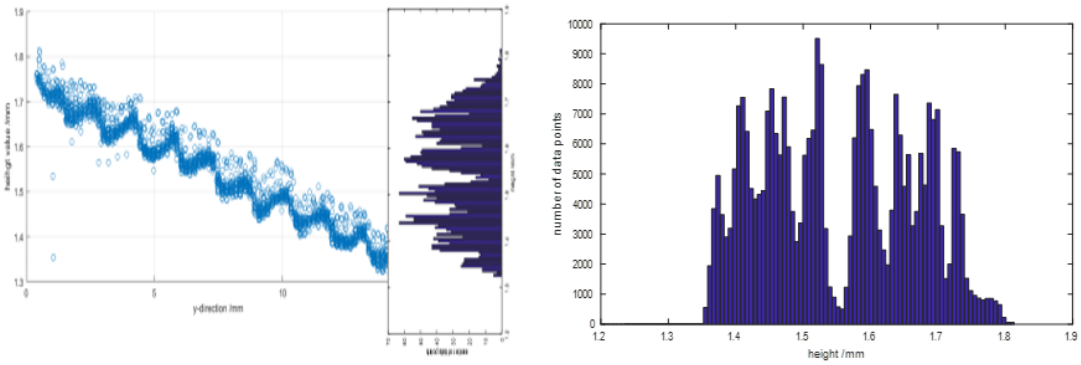

Figure 4-9. Histogram: number of data points at each height value for the topography of FP.

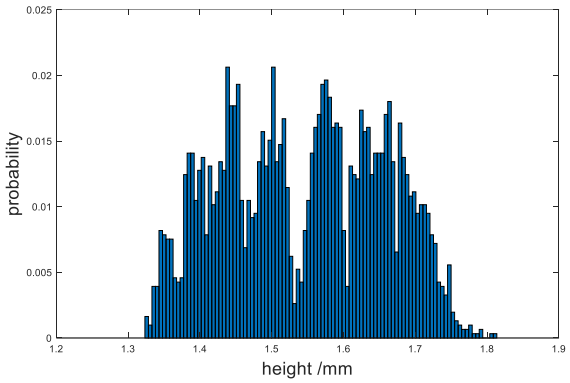

Figure 4-10. Histogram: probability distribution of the height values for topography of CMM.

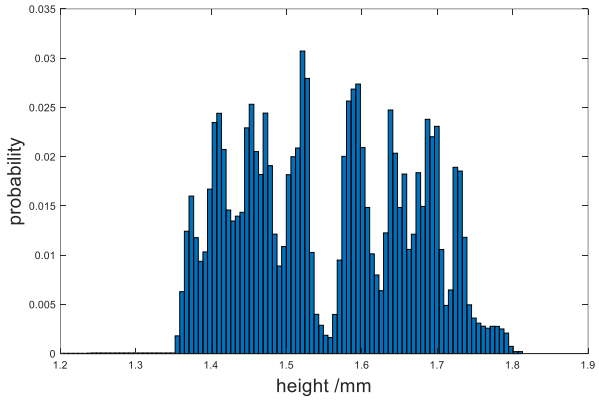

Figure 4-11. Histogram: probability distribution of the height values for topography of FP

5.0 Uncertainty Analysis

In the previous sections we went through the process of developing a fringe projection system, fringe pattern analysis algorithm, in-situ powder bed topography using FP, and the experimentation for ex-situ topography validation. However, either from the in-situ or ex-situ topography, noise is observed in the measurement result. The possible sources for those noise are uncertainty of captured image intensity and vertical calibration process. In this section, we will examine the uncertainty of the topography caused by image noise and the calibration process. In subsection 5.1, we explore the height uncertainty that is contributed by the captured light intensity. And the uncertainty from calibration process is discussed in section 5.2.

5.1 Uncertainty from Captured Intensity

During our previous experiment, we observed that the noise (uncertainty) of the captured intensity is not a constant but a function that varies with intensity. To view this effect, we project an intensity map that the intensity is varying linearly in the horizontal direction as shown in figure 5-1 on a flat surface. And we use the camera to capture 50 images of the same surface with the projected intensity map. The uncertainty for each pixel can be determined by using the T-distribution test. With a confidence interval of 95%, the observed intensity gray level for each pixel can be expressed as:

$$\bar{x} = \mu \pm \frac{s}{\sqrt{N}} \times t_{(N-1),0.975} \quad \textbf{5-1}$$

Where $\bar{x}$ is the observed intensity gray level for each pixel, μ is the mean intensity gray level, s is the standard deviation, and $N = 50$ is the number of observations for the surface, and $t_{(N-1),0.975}$ is the t-score at the DOF (degree of freedom) of $N - 1$ and the confident interval of 95%. The uncertainty for the height measurement can be then expressed as:

$$U_I = \frac{s}{\sqrt{N}} \times t_{(N-1),0.025} \quad \textbf{5-2}$$

Once the uncertainty (in the unit of gray level) for each pixel is calculated, an uncertainty map can be created and shown in figure 5-2.

It is observed that the uncertainty of brighter area is larger than the dark area. We extract the uncertainty of the horizontal center line and create the plot of uncertainty versus the captured intensity as shown in figure 5-3. We use a second order polynomial to fit the uncertainty curve. Hence, for a captured intensity value, the uncertainty can be expressed as:

$$U_I(I) = 0.000044I^2 + 0.028I + 1 \quad \textbf{5-3}$$

Where I represents the captured intensity, and $U_I(I)$ is the uncertainty for the captured intensity. The sensitivity of the phase value can be defined as partial derivatives of phase value using equation (2-8) with respect to intensity. In our FPP, we project 3 phase shifted fringe images. Thus, we must evaluate the three frames separately. Thus, the sensitivity of phase value for each

pixel can be expressed as equation 5-4. $S_i(x,y)$ is the sensitivity of the phase value with respect to the i-th frame for each pixel. Hence the sensitivity of height with respect to the captured intensity can be derived using the chain rule as shown in equation 5-5, where $K(x,y)$ is the same as equation 2-5, determined by the vertical calibration process. Lastly, the uncertainty of height value can be expressed as the sensitivity of height multiplied by the uncertainty of captured light intensity. As we are capturing the 3 frames, the uncertainty of light intensity is calculated using root square of the three frames as shown in equation 5-6.

$$S_i(x,y) = \frac{\partial \phi}{\partial I_i} = \frac{1}{1+\left(\frac{-\sum sin(\delta_i)\, I_i(x,y)}{\sum cos(\delta_i)\, I_i\,(x,y)}\right)^2}\left(\frac{cos\,(\delta_i)\sum sin(\delta_i)\, I_i(x,y)\; - sin\,(\delta_i)\sum cos(\delta_i)\, I_i(x,y)}{(\sum cos(\delta_i)\, I_i(x,y)\,)^2}\right) \quad \textbf{5-4}$$

$$U_I = \sqrt{\sum_{i=1}^{3}\left(S_i(x,y) \times u_{I_i}(x,y)\right)^2} \quad \textbf{5-5}$$

$$U_{Z|\phi}(x,y) = K(x,y) \times U_I = K(x,y) \times \sqrt{\sum_{i=1}^{3}\left(S_i(x,y) \times U_{I_i}(x,y)\right)^2} \quad \textbf{5-6}$$

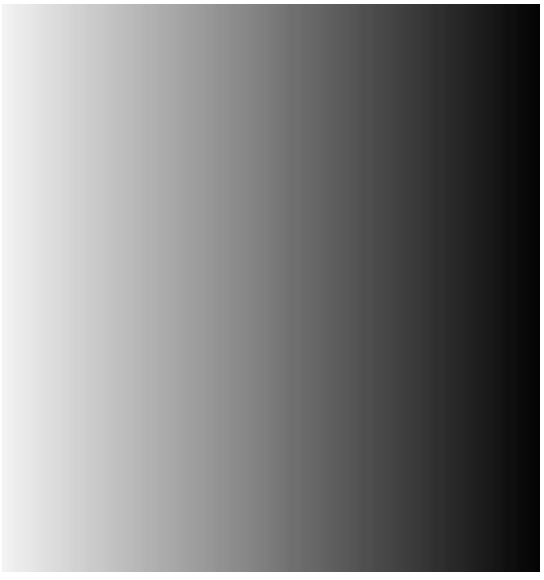

Figure 5-1. Projected imtensity map.

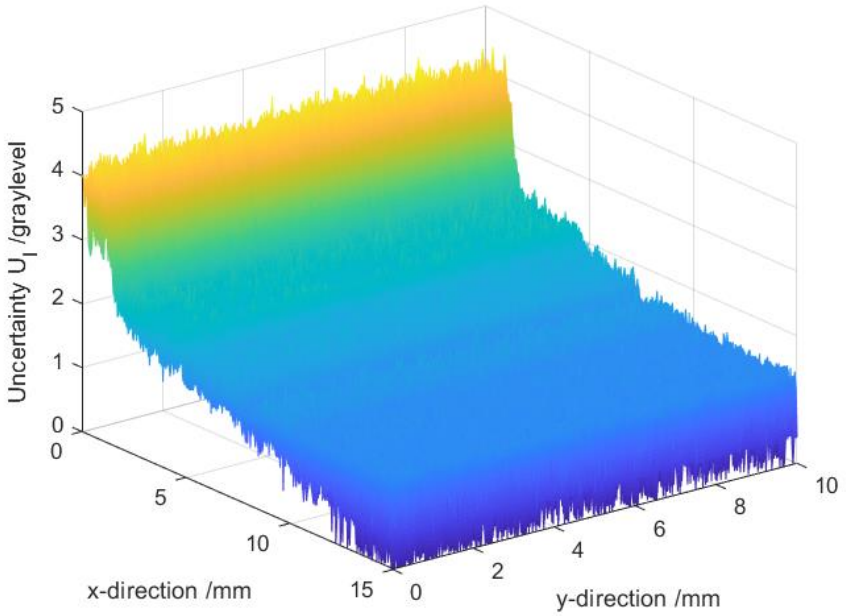

Figure 5-2. Uncertainty map obtained from the developed model.

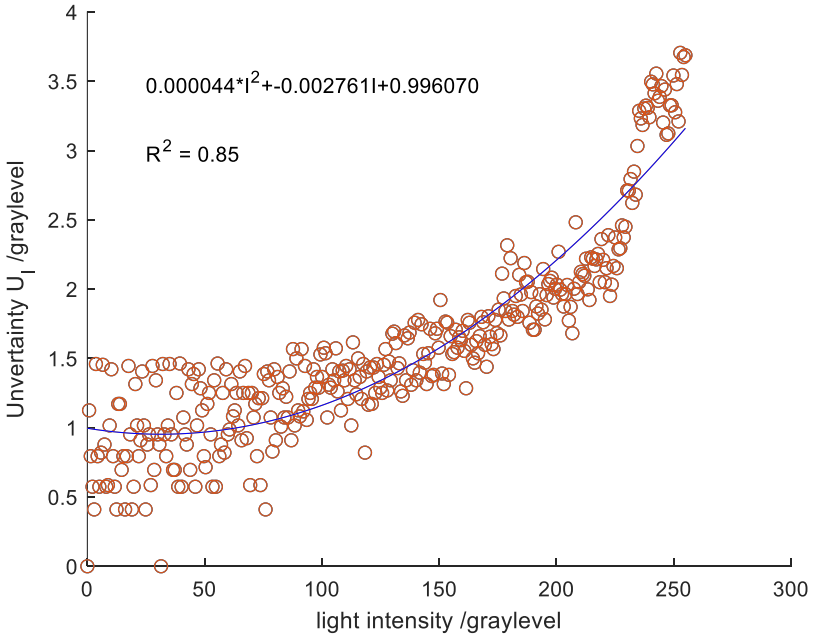

Figure 5-3. Plot of uncertainty vs. captured light intensity.

5.2 Uncertainty from Calibration Process

Another source of uncertainty in the height profile measurement is from the out of plane calibration process. In section 2, we discussed that the out-of-plane calibration is the process of converting an unwrapped phase map to a height map. In another words, it is a process of determining the parameter $K(x, y)$ for each pixel in equation (2-5). This is done by moving a flat reference plane over a range that covers the height variation of the powder bed. For our system, we use the first powder layer as the reference plane and move the build stage to ten different height positions with increments of 0.1 mm. We define the first height position as 0 mm and move the build stage down to -0.1 mm, -0.2mm, …, -1.0 mm. The unwrapped phase maps are calculated for the ten height positions. For each pixel, the phase values and their corresponding height are fit to a straight line, and the slope, which has unit of millimeter per radian (mm/rad), is obtained and assigned to $K(x, y)$ in equation (2-5). As shown in figure 2-11, a linear regression is used to fit the data points at each pixel. To construct confidence intervals around the calculated slope $K(x, y)$, we use t-distribution and $n - 2$ =8 (we used 10 height positions to evaluate the slope) degrees of freedom (Morrison, 2014). The 95% confidence intervals (CI) on the calculated slope can be expressed as:

$$95\%\ CI\ on\ K(x,y): K\ \pm t_{0.025,8}\ \times S_K \qquad \textbf{5-7}$$

Where $t_{0.025,8}$ is the t-score at the DOF (degree of freedom) of 8 and the confident interval of 95%, and S_K is the standard deviation of the K value can be determined by:

$$S_k = \sqrt{\frac{s_{y,x}^2}{SS_{xx}}} \quad \textbf{5-8}$$

Where $s_{y,x}^2$ is the variance of the $y(x)$ which is the dependent variables (it is the height positions in our case, see figure 2-13) and is expressed as:

$$s_{y,x}^2 = \left(\frac{1}{n-2}\right)\sum_{i=1}^{n}(y_i - \hat{y}_i)^2 \quad \textbf{5-9}$$

Where $\hat{y}$ is the linear regression value of the height position (calculated from the fitting line equation), and SS_{xx} is expressed as:

$$SS_{xx} = \sum_{i=1}^{n}(x_i - \bar{x}) \quad \textbf{5-10}$$

Where $\bar{x}$ is the mean of independent variables (it is the phase value ϕ in our case, See figure 2-13. Hence, the uncertainty of the K value for each pixel is:

$$U_K(x,y) = t_{0.025,8} \times S_K(x,y) \quad \textbf{5-11}$$

Thus, the uncertainty contributed from the calibration process can be mathematically expressed as:

$$U_{Z|K}(x,y) = \frac{\partial Z(x,y)}{\partial K(x,y)} \times U_K(x,y) = \phi(x,y) \times U_k(x,y) \quad \textbf{5-12}$$

5.3 Conclusion for Uncertainty Analysis

As discussed in subsection 5.1 and 5.2, we consider two sources of uncertainty, captured intensity and calibration. To combine the two aspects of the uncertainty, the root square is used, and the equation is expressed as:

$$U_Z(x,y) = \sqrt{U_{Z|K}(x,y)^2 + U_{Z|\phi}(x,y)^2} \quad \textbf{5-13}$$

$$U_{Z|K}(x,y) = \phi(x,y) \times U_k(x,y) \quad \textbf{5-14}$$

$$U_{Z|\phi}(x,y) = K(x,y) \times \sqrt{\sum_{i=1}^{3} \left(S_i(x,y) \times U_{I_i}(x,y)\right)^2} \quad \textbf{5-15}$$

Figure 5-4 shows the uncertainty map that calculated from the above mathematical model for a powder layer surface. The average uncertainty of the FP height measurement across the whole plane is 2.86 um.

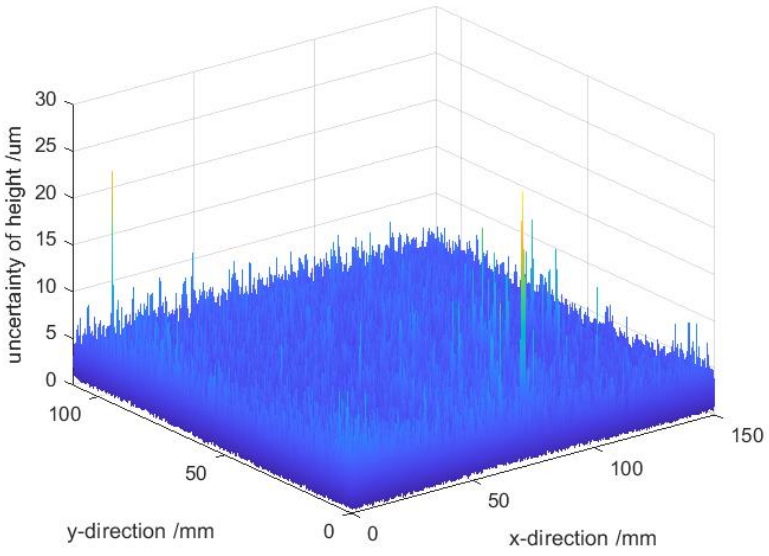

Figure 5-4. Calculated uncertainty map.

To validate the uncertainty analysis model, we can test the repeatability of the topography measurement of our FP system. An experiment was done by measuring the build stage surface N times, and the uncertainty for each pixel can be determined by using the T-distribution test. With a confidence interval of 95%, the measured mean height value for each pixel can be expressed as:

$$\bar{x} = \mu \pm \frac{s}{\sqrt{N}} \times t_{(N-1),0.975} \qquad \textbf{5-16}$$

Where $\bar{x}$ is the measured average height value for each pixel, μ is the mean height value of the topography, s is the standard deviation, and N is the number of measurements for the surface, and $t_{(N-1),0.975}$ is the t-score at the DOF (degree of freedom) of $N-1$ and the confidence interval of 95%. The uncertainty for the height measurement can be then expressed as:

$$u_z = \frac{s}{\sqrt{N}} \times t_{(N-1),0.025} \quad \textbf{5-17}$$

In our experiment, we took 20 measurements ($N = 20$) for the same flat surface. Figure 5-5 below shows the uncertainty map for each pixel. The average of the measured uncertainty is 4.73 μm. It is observed that the measured average uncertainty is larger than the calculated uncertainty. However, we can see that the standard deviations of the two uncertainty matrices (figure 5-4 and figure 5-5). So, to compare the two uncertainty matrices, we apply normal distribution test. The z-score can be expressed as:

$$z = \frac{\bar{x}_{measured} - \bar{x}_{calculated}}{S_{measured}} = \frac{4.73\mu m - 2.86\mu m}{1.31\mu m} = 1.43 \quad \textbf{5-18}$$

where $\bar{x}_{measured}$ is the average of measured uncertainty, $\bar{x}_{calculated}$ is the calculated uncertainty, and $S_{measured}$ is the standard deviation of the measured uncertainty. From a z-test table, the critical z-score with a confidence interval of 95% is 1.65, which is larger than the calculated z-score in equation (5-18). Thus, we can conclude that the two uncertainty matrices are statistically equal.

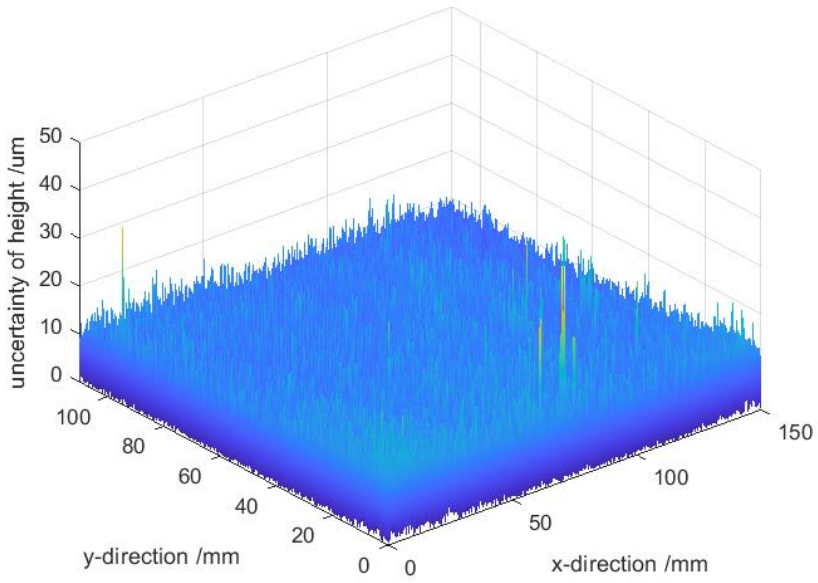

Figure 5-5. Measured uncertainty map.

6.0 Conclusion

Metal Additive manufacture is capable of creating complex geometrical products. However, it suffers from fabrication defects such as porosity and inconsistent mechanical properties. Due to lack of real time control strategies, the laser power, scan speed, and meltpool dimensions are all source of such issues. Thus, in-situ metrology has great potential of providing operators the knowledge of the manufacturing process so that make it possible for activating feedback control to compensate and even correct the detected anomalies. Fringe projection profilometry can provide a in-situ monitoring method that capture the three-dimensional information of the powder bed and printed area for LPBF process. In this work, we developed a fringe projection system with implementing a modified phase unwrapping algorithm to obtain the height information of each layer for LPBF process.

To develop a fringe projection system, a DLP LightCrafter Projector and a Flea3 CMOS camera are used. The field of view of the developed system is 110 mm by 150 mm. The principals of fringe projection profilometry are discussed in detail in this thesis. To reduce the periodical error in the height measurement, we implement a 2D Fourier filter in the phase unwrapping process and the in-situ height profile of fatigue bar show the improvements from the modified phase unwrapping process. The height profile produced by the developed projection system can provide us the height variation of the powder bed and actual layer thickness during the printing process. An experiment of measuring the ex-situ step surface validates the measurement capability of the system. From this experiment we can conclude that the height measurement resolution is below 40 μm. Finally, a mathematical model for uncertainty analysis is developed to evaluate the accuracy of the height measurement result.

7.0 Future Improvements

As declared in the introduction, one of the goal for this project is to achieve a heihgt measurement of 10 μm using our FP system. A ex-situ experiment of measuring the step surface with 40 μm step increment has been conducted to assertain that currently the height resolution can achieve 40 μm. Thus, to further evaluate the height resolution, the main future work is to conduct an experiment of measuring the step surface with 10 μm step increments and compare the measured topography by FPP with a ground truth. Figure 7-1 shows the preliminary FP measured topography for the 10 μm step surface. A Keyence digital light optical microscope will be used to provide us the ground truth for the topography of the 10 μm step surface.

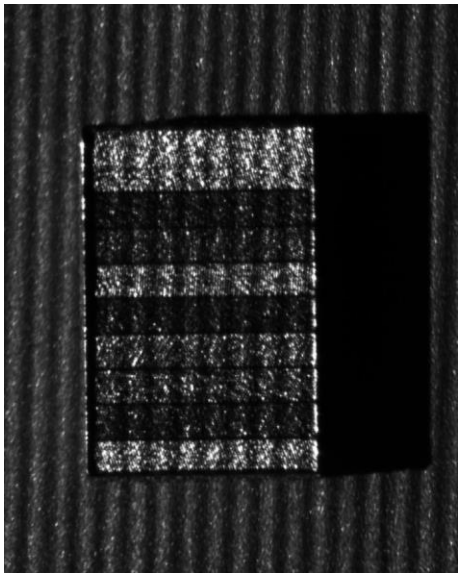

Figure 7-1. Ex-situ 10 um step surface measurement.

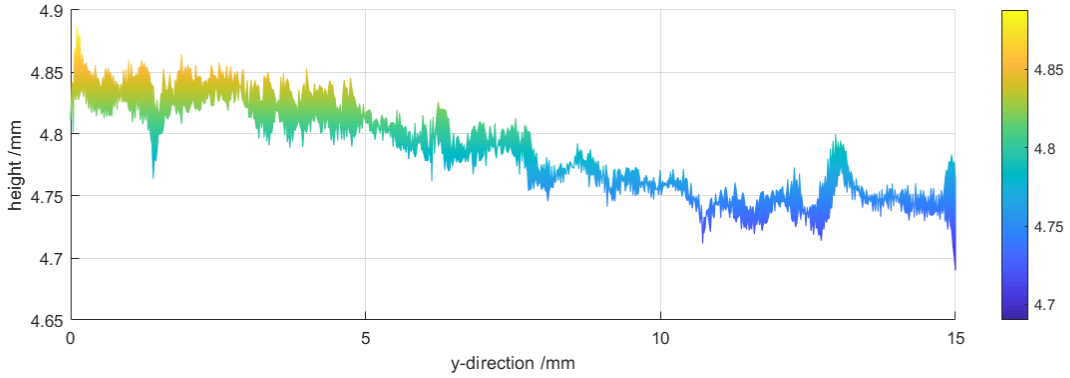

Figure 7-2. Side side view of FP measured topography of the 10 um step surface.

Another future work is the anomalies identification for the powder bed during the printing process. As the in-situ topography of each powder layer can provide us tremendous information such as printed area boundary detection, printed area height variation, and anomalies information, we are going to use the topographies of each layer to train a neural network to identify anomalies in the printed areas.

The major limitation of our FP system is that the projected light incident on the printed area will cause some over saturated issues in the captured images as shown in figure 7-3. Most of the height information are lost in the oversaturated area. Thus, we tried decrease the overall projected intensity and over saturated area reduced as shown in figure 7-4. However, there are still some over saturated pixels. As we aim to use the in-situ topographies to identify printing anomalies, this issue should be addressed. Hence, we propose to use dual projection, in which we project the fringe pattern from two angles: from the first angle, the oversaturated area will be recorded and compensated by the second angle projection, because the oversaturated areas are expected to shift when projecting from another angle.

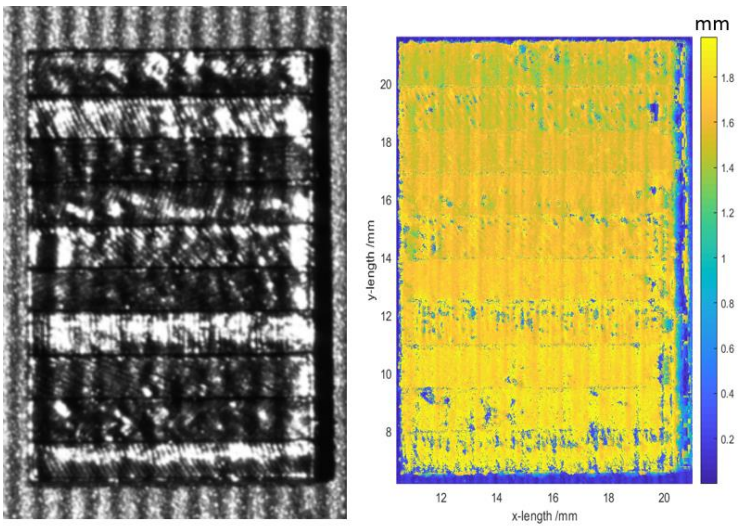

Figure 7-3. Ex-situ image for the 40 um step surface (left) and the FP measured topography (right).

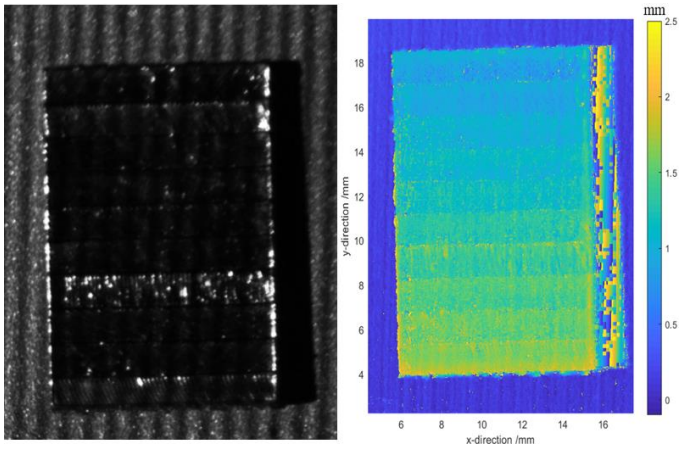

Figure 7-4. Reduced projected intensity: Ex-situ image for the 40 um step surface (left) and the FP measured topography (right)

Appendix A MATLAB Code

Phase Shifting Algorithm: calculating wrapped phase map

```
% input: path of the folder that stores the captured images
function M = p_shift(path)
n = 3; %3-step phase shifting
%read image:
fp = fullfile(path, '*.bmp'); % The image format is .bmp
img = dir(fp);
fpName = img(1).name;
imgName = fullfile(path, fpName);
II = imread(imgName);
II=rgb2gray(II);
[w,h] = size(II);
I = cell(1,n);
for k = 1:length(img)
    fpName = img(k).name;
    imgName = fullfile(myFolder, fpName);
    II = imread(imgName);
    II=rgb2gray(II);
    II=double(II);
    % Camera calibration:
    II = 2.6522e-5*II.^3 -0.0111*II.^2 + 1.9212*II +1.1274;
end
%%Calculate wrapped phase:
Y = zeros(w,h); X = zeros(w,h);
for i = 1:n
    sigma = 2*(i-1)*pi/n;
    Y = Y-(sin(sigma).*double(cell2mat(I(1,i))));
    X = X+(cos(sigma).*double(cell2mat(I(1,i))));
end
M = atan2(Y,X);
end
```

Phase Unwrapping Algorithm: Ioth's Unfolding

```
function uphi_ref = unfold(phi);
[w h] = size(phi);
uphi_ref = phi;
```

```
% unwrapped columns
    for i=1:h
        uphi_ref(:,i) = unwrap(uphi_ref(:,i));
    end
% unwrap rows
    for j=1:w
        uphi_ref(j,:) = unwrap(uphi_ref(j,:));
    end
end
```

Modified reference guided phase unwrapping model with Fourier filtering

```
function phi_u=unwrap_ref(phi,phi_ref)
    % phi_ref is reference phase map
    phi = phi +2*pi*round((phi_ref-phi)/(2*pi));
    [w,h] = size(phi);
    dphi = zeros(w, h);
    %detrend columns and rows
    for i = 1:w;
        dphi(i, :) = detrend(phi(i, :), 3);
    end
    for j = 1:h
        dphi(:, j) = detrend(phi(:, j), 3);
    end
    phi2 = phi - dphi;
    dphi = Fourier_filter(dphi);
    uphi = dphi + phi2;
    phi_u = uphi;
end
```

Fourier filtering

```
function uphi=Fourier_filter(phi);
[w,h]=size(phi);
% define filted spatial frequency
fy = 10;
fx = 25;
% define filter radius
rx = 20;
ry = 2;
% define centern point
cY=w/2+1;
cX=h/2+1;
% fast 2D fourier transform
FT=fftshift(fft2(phi));
% 1st order filtering
```

```
FT(floor(cY-fy-ry):ceil(cY-fy+ry),floor(cX-fx-rx):ceil(cX-
fx+0.5*rx))=0;
FT(floor(cY+fy-ry):ceil(cY+fy+ry),floor(cX+fx-
0.5*rx):ceil(cX+fx+rx))=0;
FT(floor(cY-fy-ry):ceil(cY-fy+ry),floor(cX+fx-
rx):ceil(cX+fx+0.5*rx))=0;
FT(floor(cY+fy-ry):ceil(cY+fy+ry),floor(cX-fx-0.5*rx):ceil(cX-
fx+rx))=0;
% 2nd order filtering
FT(floor(cY-2*fy-1.2*ry):ceil(cY-2*fy+1.2*ry),floor(cX-2*fx-
rx):ceil(cX-2*fx+rx))=0;
FT(floor(cY+2*fy-1.2*ry):ceil(cY+2*fy+1.2*ry),floor(cX+2*fx-
rx):ceil(cX+2*fx+rx))=0;
FT(floor(cY-2*fy-1.2*ry):ceil(cY-2*fy+1.2*ry),floor(cX+2*fx-
rx):ceil(cX+2*fx+rx))=0;
FT(floor(cY+2*fy-1.2*ry):ceil(cY+2*fy+1.2*ry),floor(cX-2*fx-
rx):ceil(cX-2*fx+rx))=0;
% 3rd order filtering
FT(floor(cY-3*fy-ry):ceil(cY-3*fy+ry),floor(cX-3*fx-rx):ceil(cX-
3*fx+rx))=0;
FT(floor(cY+3*fy-ry):ceil(cY+3*fy+ry),floor(cX+3*fx-
rx):ceil(cX+3*fx+rx))=0;
FT(floor(cY-3*fy-ry):ceil(cY-3*fy+ry),floor(cX+3*fx-
rx):ceil(cX+3*fx+rx))=0;
FT(floor(cY+3*fy-ry):ceil(cY+3*fy+ry),floor(cX-3*fx-rx):ceil(cX-
3*fx+rx))=0;
% 4th order filtering
FT(floor(cY-4*fy-ry):ceil(cY-4*fy+ry),floor(cX-4*fx-rx):ceil(cX-
4*fx+rx))=0;
FT(floor(cY+4*fy-ry):ceil(cY+4*fy+ry),floor(cX+4*fx-
rx):ceil(cX+4*fx+rx))=0;
FT(floor(cY-4*fy-ry):ceil(cY-4*fy+ry),floor(cX+4*fx-
rx):ceil(cX+4*fx+rx))=0;
FT(floor(cY+4*fy-ry):ceil(cY+4*fy+ry),floor(cX-4*fx-rx):ceil(cX-
4*fx+rx))=0;
% 5th roder filtering
FT(floor(cY-5*fy-ry):ceil(cY-5*fy+ry),floor(cX-5*fx-rx):ceil(cX-
5*fx+rx))=0;
FT(floor(cY+5*fy-ry):ceil(cY+5*fy+ry),floor(cX+5*fx-
rx):ceil(cX+5*fx+rx))=0;
FT(floor(cY-5*fy-ry):ceil(cY-5*fy+ry),floor(cX+5*fx-
rx):ceil(cX+5*fx+rx))=0;
FT(floor(cY+5*fy-ry):ceil(cY+5*fy+ry),floor(cX-5*fx-rx):ceil(cX-
5*fx+rx))=0;
% delete high frequency noise
FT(1:ry,floor(cX-rx):ceil(cX+rx))=0;
FT(w-ry:w,floor(cX-rx):ceil(cX+rx))=0;
```

```
% inverse fourier transform
uphi = real(ifft2(ifftshift(FT)));
end
```

Bibliography

Bourell, D. L., Leu, M. C., & Rosen, D. W. (2009). Roadmap for additive manufacturing: identifying the future of freeform processing. *The University of Texas at Austin, Austin, TX*, 11-15.

Chen, L.-C., & Huang, C.-C. (2005). Miniaturized 3D surface profilometer using digital fringe projection. *Measurement Science and Technology, 16*(5), 1061.

Chen, L. C., & Chang, Y. W. (2008). *High accuracy confocal full-field 3-D surface profilometry for micro lenses using a digital fringe projection strategy.* Paper presented at the Key Engineering Materials.

Clijsters, S., Craeghs, T., Buls, S., Kempen, K., & Kruth, J.-P. (2014). In situ quality control of the selective laser melting process using a high-speed, real-time melt pool monitoring system. *The International Journal of Advanced Manufacturing Technology, 75*(5-8), 1089-1101.

Etzion, T. (1988). Constructions for perfect maps and pseudorandom arrays. *IEEE Transactions on information theory, 34*(5), 1308-1316.

Fechteler, P., & Eisert, P. (2009). Adaptive colour classification for structured light systems. *IET Computer Vision, 3*(2), 49-59.

Fredricksen, H. (1982). A survey of full length nonlinear shift register cycle algorithms. *SIAM review, 24*(2), 195-221.

Gobert, C., Reutzel, E. W., Petrich, J., Nassar, A. R., & Phoha, S. (2018). Application of supervised machine learning for defect detection during metallic powder bed fusion additive manufacturing using high resolution imaging. *Additive Manufacturing, 21*, 517-528.

Hooper, P. A. (2018). Melt pool temperature and cooling rates in laser powder bed fusion. *Additive Manufacturing, 22*, 548-559.

Huang, L., Chua, P. S., & Asundi, A. (2010). Least-squares calibration method for fringe projection profilometry considering camera lens distortion. *Applied optics, 49*(9), 1539-1548.

Huang, P. S., Zhang, C., & Chiang, F.-P. (2003). High-speed 3-D shape measurement based on digital fringe projection. *Optical Engineering, 42*(1), 163-169.

Itoh, K. (1982). Analysis of the phase unwrapping algorithm. *Applied optics, 21*(14), 2470-2470.

Jia, P., Kofman, J., & English, C. E. (2007). Comparison of linear and nonlinear calibration methods for phase-measuring profilometry. *Optical Engineering, 46*(4), 043601.

Kemao, Q., Gao, W., & Wang, H. (2008). Windowed Fourier-filtered and quality-guided phase-unwrapping algorithm. *Applied optics, 47*(29), 5420-5428.

Leach, R. (2014). *Fundamental principles of engineering nanometrology*: Elsevier.

Liu, H., Su, W.-H., Reichard, K., & Yin, S. (2003). Calibration-based phase-shifting projected fringe profilometry for accurate absolute 3D surface profile measurement. *Optics communications, 216*(1-3), 65-80.

Liu, Y., Blunt, L., Zhang, Z., Rahman, H. A., Gao, F., & Jiang, X. (2020). In-situ areal inspection of powder bed for electron beam fusion system based on fringe projection profilometry. *Additive Manufacturing, 31*, 100940.

Moylan, S., Whitenton, E., Lane, B., & Slotwinski, J. (2014). *Infrared thermography for laser-based powder bed fusion additive manufacturing processes.* Paper presented at the AIP Conference Proceedings.

Reich, C., Ritter, R., & Thesing, J. (2000). 3-D shape measurement of complex objects by combining photogrammetry and fringe projection. *Optical Engineering, 39*(1), 224-231.

Scime, L., & Beuth, J. (2018). A multi-scale convolutional neural network for autonomous anomaly detection and classification in a laser powder bed fusion additive manufacturing process. *Additive Manufacturing, 24*, 273-286.

Vallabh, C. K. P., Y. Xiong, and X. Zhao. (2020). *In-situ Monitoring of Laser Powder Bed Fusion Process Anomalies via a Comprehensive analysis of off-axis Camera Data*. Paper presented at the ASME 2020 International Manufacturing Science and Engineering Conference, 2020. Cincinnati, Ohio, USA.

Wolberg, G. (1990). *Digital image warping* (Vol. 10662): IEEE computer society press Los Alamitos, CA.

Yagnik, J., Siva, G. S., Ramakrishnan, K., & Rao, L. K. (2005). *3D shape extraction of human face in presence of facial hair: A profilometric approach.* Paper presented at the TENCON 2005-2005 IEEE Region 10 Conference.

Zhang, B., Ziegert, J., Farahi, F., & Davies, A. (2016). In situ surface topography of laser powder bed fusion using fringe projection. *Additive Manufacturing, 12*, 100-107.

Zhang, S., & Huang, P. S. (2006). Novel method for structured light system calibration. *Optical Engineering, 45*(8), 083601.

Zhou, G., Li, Z., Wang, C., & Shi, Y. (2009). A novel method for human expression rapid reconstruction. *Tsinghua Science & Technology, 14*, 62-65.

Zuo, C., Feng, S., Huang, L., Tao, T., Yin, W., & Chen, Q. (2018). Phase shifting algorithms for fringe projection profilometry: A review. *Optics and Lasers in Engineering, 109*, 23-59.

zur Jacobsmühlen, J., Kleszczynski, S., Schneider, D., & Witt, G. (2013). *High resolution imaging for inspection of laser beam melting systems.* Paper presented at the 2013 IEEE international instrumentation and measurement technology conference (I2MTC).